Intercomparison of very high-resolution surface soil moisture products over Catalonia (Spain)

Nadia Ouaadi, Lionel Jarlan, Michel Le Page, Mehrez Zribi, Giovani Paolini, Bouchra Ait Hssaine, Maria Jose Escorihuela, Pascal Fanise, Olivier Merlin, Nicolas Baghdadi, et al.

Remote Sensing of Environment 309 (2024) 114225

Contents lists available at ScienceDirect

Remote Sensing of Environment

journal homepage: www.elsevier.com/locate/rse

Intercomparison of very high-resolution surface soil moisture products over Catalonia (Spain)

Nadia Ouaadi [a,b,d,*], Lionel Jarlan [a], Michel Le Page [a], Mehrez Zribi [a], Giovani Paolini [c], Bouchra Ait Hssaine [d], Maria Jose Escorihuela [c], Pascal Fanise [a], Olivier Merlin [a], Nicolas Baghdadi [e], Aaron Boone [b]

[a] CESBIO, University of Toulouse, IRD/CNRS/UPS/CNES, Toulouse, France
[b] GMME/SURFACE, Meteo-France/CNRM, Toulouse, France
[c] IsardSAT, Parc Tecnològic Barcelona Activa, Barcelona, Spain
[d] CRSA, Mohammed VI Polytechnic University, Ben Guerir, Morocco
[e] INRAE, TETIS, University of Montpellier, AgroParisTech, Montpellier, France

ARTICLE INFO

Edited by Jing M. Chen.

Keywords:
Surface soil moisture
Very high-resolution
Remote sensing
C-band
L-band
Evaluation
Semiarid region

ABSTRACT

The surface soil moisture (SSM) is a key variable for monitoring hydrological, meteorological and agricultural processes. It can be estimated from active and passive microwave remote sensing data. While coarse-resolution SSM products (> 1 km) have already been evaluated for a large range of ecosystems, such assessments lack very high-spatial-resolution SSM products, although they are increasingly available thanks to very high-resolution radar data or disaggregation methods applied to coarse-scale products. Within this context, the aim of the current study is to carry out, for the first time, an intercomparison of high-spatial resolution SSM products using a large in situ SSM database collected from 33 fields located in the Ebro basin (Spain) that were cultivated with different crops and irrigated using different techniques. Three products are considered: (i) SSM_{Theia} at the field scale derived from Sentinel-1 and Sentinel-2 data using a machine learning algorithm; ii) SSM_{ρ} at 50-m resolution derived from the Sentinel-1 data using both the backscattering coefficient and the interferometric coherence based on the inversion of a simple radiative transfer model; and iii) $SSM_{SMAP20m}$ at 20-m resolution obtained by disaggregating SMAP SSM using Sentinel-3 and Sentinel-2 data. The statistical metrics computed on the whole database show that the two Sentinel-1 products outperform the disaggregated approach and that the SSM_{ρ} product exhibits better statistical metrics than the SSM_{Theia} product. This is mainly attributed to the inability of the SSM_{Theia} approach to retrieve SSM >0.3 m^3/m^3. The correlation coefficients are >0.4 (up to 0.8) for 72%, 40% and 27% of the fields using SSM_{ρ}, SSM_{Theia} and $SSM_{SMAP20m}$, respectively. Similarly, 80% of the fields had RMSE values between 0.06 m^3/m^3 and 0.1 m^3/m^3 using SSM_{ρ} product against 36% using SSM_{Theia} and 27% using $SSM_{SMAP20m}$. In addition, the time series analysis showed that $SSM_{SMAP20m}$ was able to detect large-scale wetting events such as rainfall that impacted the whole SMAP pixel while irrigation at the field scale was not detected, mainly because the very high-resolution Sentinel-2 data used for the disaggregation of Sentinel-3 land surface temperature were not related to the hydric status of the surface. The results show that while both Sentinel-1 products perform reasonably well for cereals and, to a lesser extent, for annuals, a drastic drop of the metrics is observed for tree crops. Finally, the spatial SSM pattern over the study area is also better depicted by the Sentinel-1 products than by the $SSM_{SMAP20m}$ by comparison to the airborne GLORI GNSS-R (Global Navigation Satellite System Reflectometry) SSM maps. This study highlights the limitations of SSM products over tree crops and provides insights for improving irrigation scheduling at the field scale.

1. Introduction

Surface soil moisture (SSM) has been identified as an essential climate variable (ECV) that is crucial for characterizing the Earth's climate (GCOS, 2021). It is necessary to monitor the processes at the soil-vegetation-atmosphere interface that control the water (Al-Yaari et al., 2019; Koster et al., 2004; Li et al., 2019; Wang and Dickinson, 2012), energy (Ait Hssaine et al., 2018; Diarra et al., 2017; Gokmen et al., 2012;

* Corresponding author at: CESBIO, University of Toulouse, IRD/CNRS/UPS/CNES, Toulouse, France.

https://doi.org/10.1016/j.rse.2024.114225
Received 18 October 2023; Received in revised form 13 May 2024; Accepted 22 May 2024

Jiang et al., 2014; Kustas et al., 1998; Li et al., 2006) and carbon (Ahlström et al., 2015; Jung et al., 2017; Wang et al., 2014) budgets. However, estimating SSM is a complex task because of its high spatio-temporal variability (Brocca et al., 2010; Moran et al., 2004). At the local scale, SSM can be accurately obtained from in situ measurements either by gathering soil samples (gravimetric method) or by automatic sensors (Dobriyal et al., 2012; Vereecken et al., 2014; Walker et al., 2004b). SSM can also be predicted with land surface models using a set of input data, including meteorological forcing and model variables and parameters related to soil and vegetation characteristics (Koster et al., 2009; Nijssen et al., 2001), which are likely to be uncertain, limiting the accuracy of SSM predictions.

Remote sensing microwave data can provide frequent large-scale measurements (Karthikeyan et al., 2017). Their use for estimating SSM is owing to their sensitivity to the water content of the target, which in turn is related to its dielectric properties (Schmugge, 1978; Ulaby et al., 1986). Consequently, the surface emission measured by radiometers (passive) or the backscattering coefficient measured by scatterometers and SARs (active) are widely used to retrieve SSM. Given their insensitivity to atmospheric perturbations, microwave missions have been the subject of considerable investments, as demonstrated by the large number of satellites and derived products that have been made available to date. Radiometers have been used since the early 1980s (Schmugge, 1983; Ulaby and Long, 2014), but the first mission dedicated to SSM monitoring was the ESA's L-band Soil Moisture and Ocean Salinity satellite (SMOS) (Kerr et al., 2016, 2001), which was launched in 2009, followed by NASA's L-band Soil Moisture Active and Passive (SMAP) in 2014 (Entekhabi et al., 2010). Prior to the launch of SMOS, C-band AMSR-E data were also used to provide SSM products (Njoku, 2004; Njoku et al., 2003). Active microwave observations have also been used to retrieve SSM using scatterometers that were primarily designed to measure wind speeds and directions over the ocean (Wagner et al., 2013, 1999). Interestingly, the continuous acquisition of scatterometer data since the launch of ERS-1 in 1992 has produced long time series of coarse-scale SSM products (Wagner et al., 2003; Wagner et al., 2013).

Although global, the abovementioned passive and active products are characterized by medium to coarse spatial resolutions (>1 km). Such resolution is useful for global applications such as climate studies and large-scale drought monitoring. In contrast, they are not appropriate for agricultural decision support at the field scale that require information at a resolution equal or lower than the size of the field such as irrigation timing and amount (Le Page et al., 2023; Massari et al., 2021; Ouaadi et al., 2021b), biophysical variables (Bériaux et al., 2015; Hosseini et al., 2015), evapotranspiration (Ait Hssaine et al., 2021), crop yields (Ines et al., 2013; Mishra et al., 2021) and irrigation or fertilizer scheduling (Le Page et al., 2014; Subhani et al., 2012). Peng et al. (2021) reviewed the different key applications of SSM products and emphasised the need for global operational products, typically with 100-m resolution. However, finer resolutions (<100 m) are generally required in many regions of the world due to the dominance of very small fields, which can be as small as 0.1 ha (Ameur et al., 2020; Defourny et al., 2019; Dobermann et al., 2003; Ouaadi et al., 2021a; Ritzema et al., 2008; Weiss et al., 2020). Indeed, Lesiv et al. (2019) showed that 23% of fields on the globe have areas of <0.64 ha. In particular, 50%, 53% and 13% of fields are smaller than 0.64 ha in Africa, Asia and Europe, respectively. Very high spatial resolutions are also required to assess the intraplot variability for precision agriculture. For example, several studies have highlighted the need for very high spatial resolution data to estimate the spatial variability of crop growth and yield within a given field (Bouras et al., 2023; Ines et al., 2013). This has prompted numerous studies to develop methods for estimating SSM at very high spatial resolution. Indeed, several attempts have been made to estimate SSM from reflectances in the shortwave infrared (SWIR) band (approximately 1500–2300 nm) and other bands based on thermal infrared data (c.f. reviews by Li et al. (2021) and Zhang and Zhou (2016)). Shortwave infrared reflectance approaches are based on water absorption bands to establish relationships between either reflectances or indices such as the normalized difference water index (NDWI, computed from the near infrared and SWIR reflectances) and SSM. Thermal infrared (TIR) approaches rely mainly on sub-diurnal observations of land surface temperature (LST) to estimate the soil thermal inertia, which is indirectly linked to its water content (Verhoef, 2004). More complex approaches based on solving the surface energy budget have also been investigated (Van Den Hurk, 2001). However, these approaches are mostly limited by the shallow penetration depth of electromagnetic waves in these wavelength domains, thereby restricting their applicability to bare or sparsely covered soils and to cloud-free conditions (Kerr, 2007; Peng et al., 2021). In contrast, microwave-based approaches are promising and can be grouped into two main categories: (i) direct inversions of very high-resolution radar data and (ii) downscaling of the coarse SSM products mentioned above. The downscaling of coarse products is widely addressed in the literature using various statistical, machine learning or physical approaches. The concept behind downscaling is to compute a very high-resolution factor using auxiliary data obtained from sensors with high spatial resolution. This factor is then used to improve the coarse spatial resolution of the original SSM product (Peng et al., 2017). Note that downscaling techniques have been used extensively to downscale SSM data up to 1 km (e.g., Choi and Hur, 2012; Merlin et al., 2013; Peng et al., 2017; Sabaghy et al., 2020), but these techniques have recently been adopted to achieve even higher spatial resolutions. For instance, LANDSAT LST combined with NDVI data from either LANDSAT or Sentinel-2 have been used to disaggregate SSM data at up to a 100-m resolution (Merlin et al., 2013; Ojha et al., 2019; Paolini et al., 2022a). SAR data were also used, as in the recent study by Ojha et al. (2021), who used Sentinel-1 data to obtain field-scale SSM from the previously downscaled SMAP product at 100-m resolution. However, SSM can be estimated directly from SAR data. Indeed, SAR imaging radars have a resolution of a few meters (RadarSAT, ENVISAT, and Sentinel-1), enabling very high-resolution mapping of SSM (Karthikeyan et al., 2017; Walker et al., 2004a). In fact, SARs are currently the only sensors capable of providing both the spatial resolution and temporal coverage required for field-scale applications (Li et al., 2021; Moran et al., 2004). Given the complexity of the radar response involving a mixture of ground and canopy contributions, the retrieval of SSM requires the use of backscattering models. Indeed, most of the studies aiming to retrieve SSM from SAR data rely on a vegetation backscattering model (e.g., Attema and Ulaby, 1978; Karam et al., 1992; Picard and Toan, 2002; Ulaby et al., 1990) coupled to a bare soil backscattering model (e.g., Dubois et al., 1995; Fung et al., 1992; Oh et al., 1992) to disentangle the contributions from each other. Using these models and SAR data, several approaches have been proposed (Bai et al., 2017; Bao et al., 2014; El Hajj et al., 2017; Gherboudj et al., 2011; He et al., 2014; Ouaadi et al., 2020).

Intercomparison studies are of prime importance to assess product performance under different climate and vegetation conditions as well as to highlight weaknesses that can be improved (Al-Yaari et al., 2019). Coarse-scale products have received considerable attention, with extensive literature dedicated to product assessments and intercomparisons (e.g., Al-Yaari et al., 2019; Brocca et al., 2011; Gruhier et al., 2010; Kim et al., 2018; Qu et al., 2021; Rüdiger et al., 2009; Yin et al., 2019). In contrast, there is a lack of similar studies on high spatial resolution products that should be better suited for field-scale agricultural applications. In this context, the aim of this study is to perform an intercomparison of three high spatial resolution SSM products, two of which are based on the inversion of Sentinel-1 data (El Hajj et al., 2017; Ouaadi et al., 2020), and one relies on the disaggregation of SMAP products (Paolini et al., 2022a). These three products have shown encouraging results for various applications, including the classification of different irrigation systems at the field scale (Paolini et al., 2022b), the retrieval of irrigation timing and/or amounts (Le Page et al., 2020; Ouaadi et al., 2021) and the mapping of evapotranspiration (Ait Hssaine et al., 2021). To this end, a large database of in situ SSM measurements

was collected in the Ebro basin (Spain) as part of the LIAISE project (https://www.hymex.fr/liaise/).

The document is organized as follows. Section 2 presents the study area, the in situ SSM database, the satellite products and the airborne GNSS-R-derived maps (GNSS-R stands for Global Navigation Satellite System Reflectometry). Section 3 is devoted to the results of (i) the evaluation of satellite products over the entire in situ SSM database, (ii) the analysis of SSM time series and (iii) the analysis of the SSM spatial patterns. The results are discussed in Section 4, and Section 5 is devoted to drawing conclusions.

2. Materials and methods

2.1. Study area description

The study was conducted over the Ebro basin in Catalonia, Northeastern Spain (Fig. 1). The climate in the region is semiarid Mediterranean and is influenced by a continental climate. This climate is characterized by mild winters, hot summers and two rainy seasons (autumn and spring) with an annual precipitation amount of approximately 350 mm against a reference evapotranspiration of approximately 1100 mm/year (Paolini et al., 2022b).

The study area, which covers 19 × 18 km^2 (left map in Fig. 1), is located in one of the most important agricultural districts in the region. It includes an irrigated section in the northwest and a rainfed section in the southeast (cf. Section 3.3). Within the irrigated area, the SSM database was gathered for several fields located in two nearby sites named "*Prat De Boldu*" and "*Ivars*" (Fig. 1, right maps). The irrigated part is mainly supported by the Urgell canal, which is fed by Pyrenean surface reservoirs. The main irrigation technique is flooding, which is the traditional method in the region, using the old canal system. The irrigation frequency is approximately two weeks. Nevertheless, some fields are also irrigated with sprinkler and drip techniques. The irrigation frequency of these modern techniques is related to farmer schedules and crop types. The area is dominated by maize, wheat, barley and alfalfa, which are cultivated as winter and/or summer crops. Fruit trees constitute the second largest percentage of the area, and they are generally irrigated using either flood or drip techniques (Paolini et al., 2022b).

2.2. Surface soil moisture database

2.2.1. In situ measurements

SSM measurements were collected at 5-cm depth over different fields cultivated with different crops and irrigated using multiple techniques. The fields were monitored during the winter and/or summer agricultural seasons in 2021, depending on the crop. The SSM database will soon be available on the HILIAISE project website (https://www.aeris-data.fr/). The rainfall amounts were obtained from the Ruralcat portal (https://ruralcat.gencat.cat/agrometeo.estacions), which provides meteorological data from several weather stations across Catalonia. The Tornabous station, located approximately 7 km away, is the closest station to the study site.

2.2.1.1. Prat De Boldu. SSM data were collected automatically using a low-cost sensor network (Fig. 2a and b) which is composed of buried sensors connected to a data logger called LoNIM (Low-cost Network for Environmental Monitoring), which was designed at CESBIO (https://www.cesbio.cnrs.fr/). The data were acquired with hourly time steps for 11 stations installed across different fields. The stations were connected to two gateway stations (Fig. 2c), allowing the reception and storage of data before it was transmitted to a server via the mobile network. The 11 fields were cropped with barley, wheat, maize, peas, alfalfa and apple trees (cf. Table 1). Among the 11 fields, 5 were summer crops monitored between the end of May and the end of September, and 5 were winter crops monitored between the end of March and the end of May. The field planted with apple trees was monitored from the end of March to the end of September 2021. The measurements were calibrated

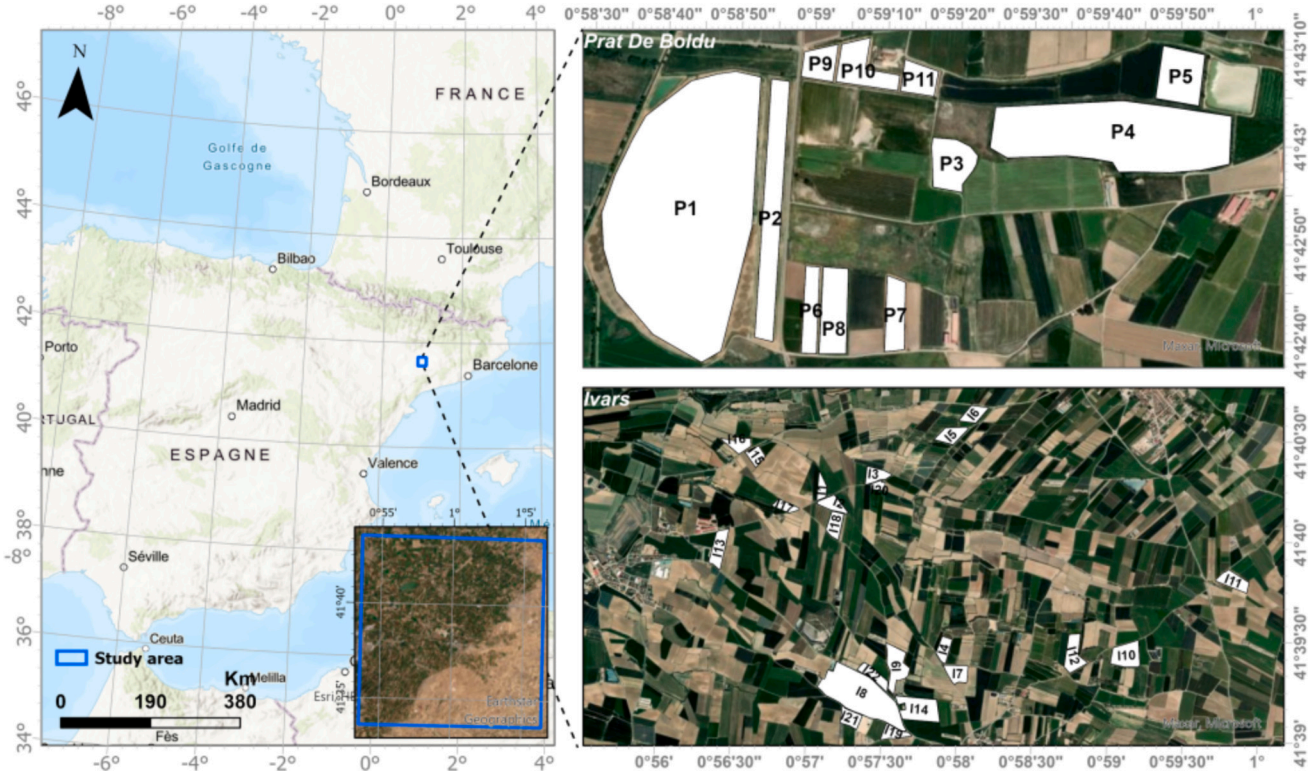

Fig. 1. Locations of the two sites, *Prat De Boldu* and *Ivars* (maps on the right), in the study area (delimited by the blue rectangle on the left map) in the Ebro basin in Catalonia, Spain. (For interpretation of the references to colour in this figure legend, the reader is referred to the web version of this article.)

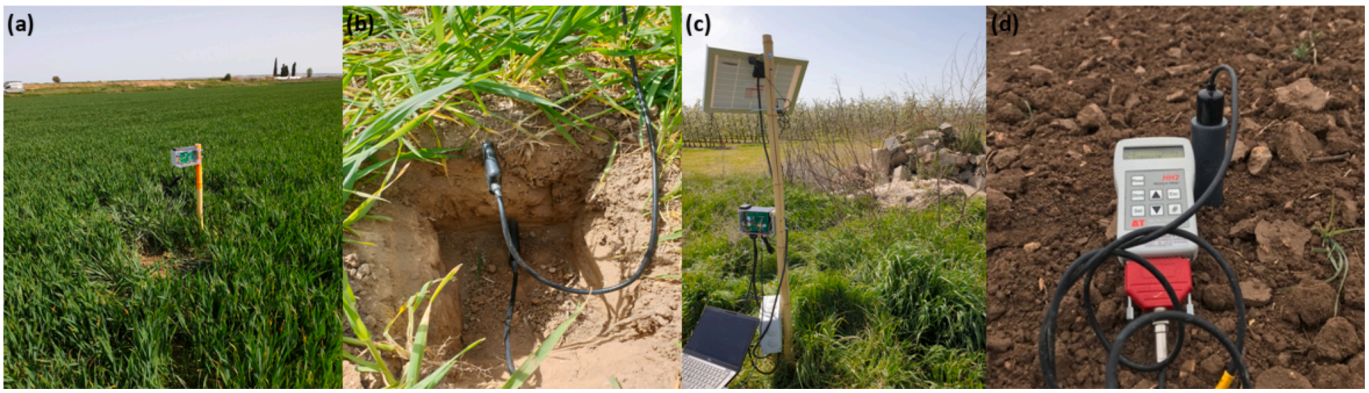

Fig. 2. Low-cost network for environmental monitoring (LoNIM) station (a) installed over a wheat field at a depth of 5 cm (b). (c) A picture of a gateway station. (d) The Thetaprobe sensor used to collect SSM over the *Ivars* site.

Table 1
General information about *Prat De Boldu* fields monitored during 2021.

	P1	P2	P3	P4	P5	P6	P7	P8	P9	P10	P11
Season	Winter	Winter	Winter	Winter	Winter	Summer	Summer	Both	Summer	Summer	Summer
Crop	Barley	Pea	Alfalfa	Barley	Wheat	Maize	Maize	Apple	Maize	Maize	Maize
Irrigation	Sprinkler	Sprinkler	Flood	Sprinkler	Flood	Flood	Flood	Flood	Flood	Flood	Flood
Area (ha)	30	4.8	1.4	13	2	1	1.3	2.1	0.8	1.5	0.9

using data from a station located close to the studied fields.

2.2.1.2. Ivars. The SSM database at the *Ivars* site was collected manually during field campaigns that were scheduled during the extensive observation period of the HILIAISE project, which took place from July 15 to July 28, 2021. SSM was measured using Thetaprobes (Fig. 2d) that were already calibrated over the study area. The field campaign included 22 fields cropped with wheat, maize, alfalfa, pear and apple trees that were irrigated using the flood or drip technique. The field sizes ranged between 0.8 and 22 ha. For each field and for each date, between 10 and 30 measurements were collected at distributed locations in the field and then averaged to provide a representative field value. The field campaigns were carried out independently of the Sentinel-1 time overpass.

2.2.2. Satellite surface soil moisture products

2.2.2.1. Theia product. The Theia pole (https://www.theia-land.fr/) provides SSM maps (named hereafter SSM_{Theia}) at the field scale with a temporal resolution of 6-day using Sentinel-1 A & B. The land use maps are first used to extract the agricultural area, and then the NDVI is used to segment the fields based on a mean-shift segmentation algorithm (Cheng, 1995). The SSM for each field was estimated using the algorithm described in El Hajj et al. (2017), which combines Sentinel-1 and Sentinel-2 data by using an artificial neural network algorithm. The mean values of the backscattering coefficients (at 20 m resolution) and NDVI (at 10 m resolution) are first computed for each field and then used to estimate SSM. A backscattering model is used to account for the contributions of the soil and of the vegetation by coupling (i) a vegetation backscattering model named the water cloud model (WCM; Attema and Ulaby (1978)) using NDVI from Sentinel-2 as the vegetation descriptor and (ii) the soil backscattering model named the modified integral equation model (MIEM; Baghdadi et al. (2011)), which integrates a semiempirical calibration with regard to the original IEM model (Fung et al., 1992). The coupled WCM-MIEM model was calibrated using a database collected in Tunisia over wheat and grasslands. The SSM measurements ranged between 0.04 and 0.4 m^3/m^3. A synthetic dataset based on the calibrated backscattering model was produced by changing the variables and parameters of the model, namely, the incidence angle; the SSM; h_{rms} (root mean square height, a soil roughness variable, Nolin et al., 2005); and NDVI and by adding random noise. This synthetic dataset was then used to train a neural network algorithm. The algorithm was validated on a database of approximately 289 measurement points that were collected in the Occitania region in France with SSM measurements ranging between 0.07 and 0.36 m^3/m^3. The SSM was estimated with an accuracy of approximately 0.05–0.06 m^3/m^3 using Sentinel-1 VV polarization data. In particular, the authors reported these good results for moderately covered soils, typically with NDVI lower than 0.75, because of the limited penetration of the C-band in dense canopies.

2.2.2.2. Coherence product. The coherence product (hereafter named SSM_{ρ}) is provided at approximately 50-m resolution every 6-day using Sentinel-1 A & B. SSM_{ρ} is derived from the backscattering coefficient and interferometric coherence (at approximately 50-m resolution, i.e., the size of the 15 × 3 - range x azimuth pixels of the SLC product window) using a "brute-force" algorithm. Full details on this approach can be found in Ouaadi et al. (2020). As for SSM_{Theia}, the WCM is used to simulate the canopy backscattering coefficient, while the soil backscattering model is the Oh model (Oh et al., 1992). The vegetation descriptor is the aboveground biomass derived from interferometric coherence using an empirical relationship. The coupled model was calibrated using data from wheat fields in Morocco. The SSM was retrieved by minimizing the distance between Sentinel-1 and WCM-simulated backscattering coefficient via the "brute-force" approach (Jarlan et al., 2002) by exploring a range of SSM values from 0 to 0.5 m^3/m^3 with a step of 0.0005 m^3/m^3 and an h_{rms} range from 0.7 cm to 1.5 cm. In this study, the h_{rms} range was broadened from 0.1 cm to 1.5 cm because the study fields were much smoother than the fields in Morocco that were used to calibrate the approach. Over a given field, h_{rms} is assumed to be constant throughout the season, as there is usually no soil work after sowing, and in situ measurements carried out in Morocco have shown that roughness changes are very limited during an agricultural season (Ouaadi et al., 2020). The backscattering coefficient at VV polarization was found to outperform that at VH polarization in estimating SSM. The validation of the retrieved SSM over 445 measurements collected from different wheat fields that were both irrigated

and rainfed in Morocco and Tunisia resulted in an RMSE of 0.06 m^3/m^3. The SSM measurements ranged between 0.04 and 0.5 m^3/m^3. SSM_ρ will soon be available on the HILIAISE project website (https://www.aeris-data.fr/).

2.2.2.3. SMAP20m product. The SMAP20m product (hereafter named $SSM_{SMAP20m}$) is the enhanced SMAP SSM product with a 9-km pixel size that is disaggregated at a 20-m resolution using the modified DisPATCh algorithm (Merlin et al., 2012) and Sentinel-3 and Sentinel-2 data. First, daily LST data from Sentinel-3 with a 1-km resolution are downscaled to 20 m using the Sentinel-2 reflectances via an ensemble decision tree method (Guzinski and Nieto, 2019). Second, the 20-m Sentinel-3 output product is used to downscale the enhanced 9-km SMAP product. The use of 9 km over 36 km is justified first by the gridding of the product at 9 km, which avoids the boxy artefacts that appear in the disaggregation process. In addition, the interpolation technique adopted explicitly uses antenna pattern information and a finer mesh to better capture the high spatial frequency information in the original radiometer measurements that were oversampled in the scan direction. As a result, although the native resolution remains at approximately 36 km, the images of the 9-km product reveal enhanced visual features that are not apparent in the standard product (Chan et al., 2018). The product provides SSM maps every 2–3 days in the absence of clouds. The $SSM_{SMAP20m}$ approach is described in detail in Paolini et al. (2022a). The DisPATCh algorithm consists mainly of two steps. First, very high-resolution thermal and optical data are used to derive the soil evaporative efficiency (SEE), which is then used in a linear formula to downscale SSM. DisPATCh is modified for application to densely vegetated areas by replacing SEE with the temperature vegetation dryness index (TVDI) over the pixels where transpiration dominates the evapotranspiration flux (meaning high NDVI values), thus assuming that SSM is linked to the root zone soil moisture. The authors reported an improvement in the 20-m SSM downscaled product at the field scale using $SSM_{SMAP20m}$ products compared to the coarser DisPATCh product at 1 km, where increases in Pearson's correlations of 17% and 40% were observed for two validation fields in Spain. The $SSM_{SMAP20m}$ product can be obtained upon request from the authors.

Note that field-averaged values are computed for SSM_ρ and $SSM_{SMAP20m}$ to be comparable to SSM_{Theia} provided at this scale. Concerning the timing, in situ measurements of the automatic stations (*Prat De Boldu* database) are extracted at the time of satellite overpass, while for *Ivars*, only data collected on the days of satellite overpass are used.

2.2.3. GNSS-R GLORI maps

The GLORI maps represent SSM (hereafter named SSM_{GLORI}) obtained from airborne GNSS reflectances. Measurements were acquired in the L-band with the GLORI instrument (Motte et al., 2016) during three flights that were scheduled over the study area as part of the LIAISE project campaign in July 2021 using the French research aircraft ATR-42. Each flight lasted approximately 4 h between 10 h and 14 h. The direct and reflected signals were acquired by two active GPS antennas mounted below and above the aircraft to ensure that several parallel passages covered the maximum area. The analysis was based on the coherent component of the reflected signals. The reflectivity measured in copolarization (right–right) was used to derive the SSM maps used in this study given the better performance compared to the cross-polarization (right–left) reflectivity. SSM was derived from the reflectivity by means of an inversion approach that uses a semiempirical model requiring the NDVI as input. The model parameters were calibrated using the *Ivars* SSM dataset. The maps are produced at 100-m resolution for three dates corresponding to three flights on July 22, July 27 and July 28 (available at https://www.aeris-data.fr/). Details on the SSM retrieval algorithm and validation can be found in Zribi et al. (2022). The two maps from July 22 and July 27 are used in Section 3.3 to compare the spatial SSM pattern over the study area with the 3 satellite products.

3. Results

In this section, the satellite products are intercompared and evaluated against in situ measurements as follows: (i) a global analysis using the entire database from both sites; (ii) a detailed analysis of the statistical metrics for each field over *Prat De Boldu* by development stages; and (iii) a time series analysis. The last part of the section is devoted to the analysis of the spatial pattern of the SSM maps over the study area.

3.1. Evaluation of satellite SSM products at the field scale using in situ measurements

Scatterplots obtained by comparing satellite products to in situ measurements over *Prat De Boldu*, *Ivars* and both sites are shown in Fig. 3. Statistical metrics (e.g., correlation coefficient – R, root mean square error – RMSE and bias) and the linear fit are also displayed. The number of points for each satellite product differs in relation to the revisit time of the sensor used to retrieve SSM. The higher number of points for $SSM_{SMAP20m}$ compared to the Sentinel-1-based products is due to the high revisit time of SMAP (2 to 3 days versus 6-day). For *Ivars*, the number of points is limited, particularly for the SSM_{Theia} and SSM_ρ products, as some field campaigns were not concomitant with the Sentinel-1 time overpass as already mentioned.

On average, SSM_ρ performed better than SSM_{Theia} and $SSM_{SMAP20m}$, particularly in terms of range. Indeed, there were almost no SSM values that exceeded 0.3 m^3/m^3 for SSM_{Theia} and, to a lesser extent, for $SSM_{SMAP20m}$, leading to lower statistical metrics than SSM_ρ. This is confirmed by the standard deviations of the products that were computed over the entire database, which are equal to 0.094, 0.068 and 0.060 m^3/m^3 for SSM_ρ, SSM_{Theia} and $SSM_{SMAP20m}$, respectively, to be compared to 0.095 m^3/m^3 for the in situ measurements. For SSM values not exceeding 0.3 m^3/m^3 (see *Ivars* site for instance), SSM_{Theia} provides good estimates that are close to those obtained by SSM_ρ with similar RMSEs and biases. The differences in terms of the correlation coefficients are only 14% (0.55 and 0.64 for SSM_{Theia} and SSM_ρ, respectively), while they are 34% over *Prat De Boldu* site. Likewise, the other metrics for SSM_{Theia} are much better for *Ivars* than for *Prat de Boldu*: improvements of 47%, 27%, 60% and 53% in terms of R, RMSE, bias and y-intercept, respectively, are observed. In contrast, some retrieved values of $SSM_{SMAP20m}$ are greater than 0.3 m^3/m^3 (see *Prat De Boldu),* but on average, they exhibit very smooth dynamics for SSM $>$ 0.25 m^3/m^3, as shown by the very low y-intercept values $<$0.1 at both sites. By considering the entire database from both sites, $SSM_{SMAP20m}$ showed lower metrics for the three products, with, in particular, lower correlation coefficients of 53% and 35% compared to SSM_ρ and SSM_{Theia}, respectively.

As SSM_{Theia} and SSM_ρ are derived from the same satellite data, similar SSM dynamics originating from the information content of the Sentinel-1 backscattering coefficient are expected. Table 2 displays the metrics obtained when comparing the products with each other. As expected, high correlations between the SSM_{Theia} and SSM_ρ products are obtained, while the correlation between the Sentinel-1-based products and $SSM_{SMAP20m}$ is low. The higher RMSE and bias values between SSM_ρ on the one hand and SSM_{Theia} and $SSM_{SMAP20m}$ on the other hand are due to the abovementioned saturation at 0.3 m^3/m^3.

To analyse the influence of vegetation cover on the accuracy of the SSM product, Table 3 summarizes the statistical metrics obtained for three NDVI ranges at both sites. The accuracy is low when vegetation covers the soil (NDVI $>$0.7), particularly for SSM_ρ and $SSM_{SMAP20m}$, due to the low contribution from bare soil and the strong attenuation of soil backscattering underneath the canopy (Ulaby et al., 1986; Greifeneder et al., 2018; Arias et al., 2022). The low statistical metrics obtained for NDVI $<$0.4 are rather surprising because the soil contribution should be

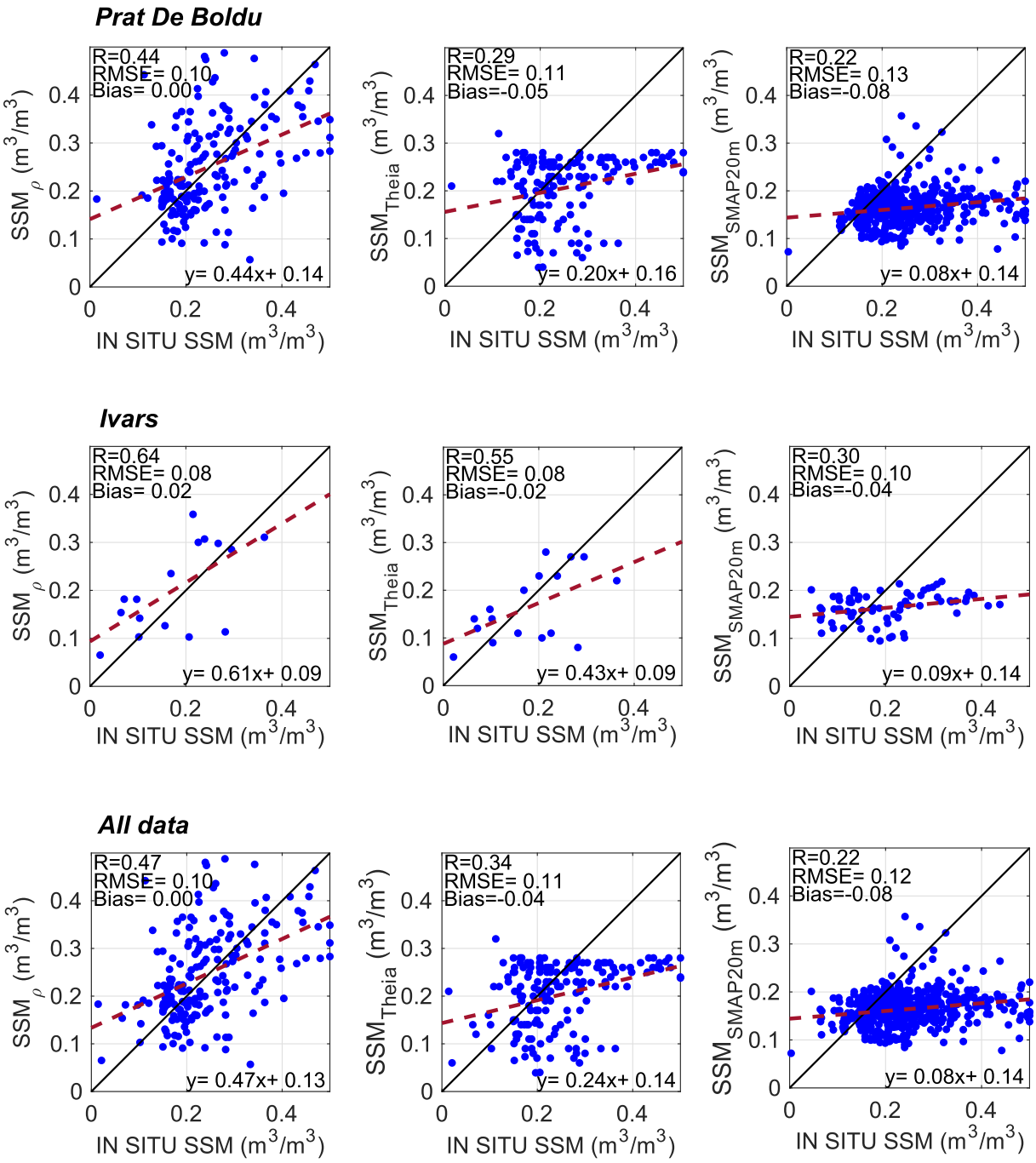

Fig. 3. Satellite-derived surface soil moisture versus in situ measurements over *Prat De Boldu*, *Ivars* and both sites. The dashed red lines are the linear regressions, and the solid black lines are Y = X. (For interpretation of the references to colour in this figure legend, the reader is referred to the web version of this article.)

Table 2
Statistical metrics obtained from intercomparing the three satellite surface soil moisture products using the entire database from *Prat De Boldu* and *Ivars* sites.

	SSM_{ρ} -SSM_{Theia}	SSM_{ρ} -$SSM_{SMAP20m}$	SSM_{Theia} -$SSM_{SMAP20m}$
R	0.69	0.33	0.42
RMSE (m^3/m^3)	0.15	0.16	0.07
Bias (m^3/m^3)	−0.10	−0.09	0.00

high for this range, but this result should be viewed with caution as the number of data points in this range (N = 20 data points, cf. Table 3) is low, with only a few points at the start and/or the end of the season for each field.

For a finer analysis of the different product behavior field by field, Fig. 4 displays the R, RMSE and bias values by field over *Prat De Boldu*. No statistical metrics are available for field P5 for the SSM_{Theia} product because the retrieval algorithm does not provide SSM values if the soil contribution is assumed to be low. *Ivars* is not included in Fig. 4 because the measurements were collected manually over a few days, so the number of data points per field is very limited. Overall, as shown in Fig. 3, the Sentinel-1 products outperform $SSM_{SMAP20m}$, and SSM_{ρ} provides better performance than SSM_{Theia}, with correlation coefficients ranging between 0.2 and 0.8 depending on the field. Specifically, the correlation coefficients are >0.4 for 72%, 40% and 27% of the fields according to SSM_{ρ}, SSM_{Theia} and $SSM_{SMAP20m}$, respectively. The bias values show underestimations for all the fields using $SSM_{SMAP20m}$

Table 3
Statistical metrics computed for three NDVI ranges for the three satellite surface soil moisture products using the entire database from *Prat De Boldu* and *Ivars* sites.

		NDVI < 0.4	0.4 ≤ NDVI < 0.7	NDVI > 0.7
SSM_{ρ}	R	0.2	0.59	0.36
	RMSE (m^3/m^3)	0.1	0.08	0.11
	Bias (m^3/m^3)	0.05	0	−0.02
	N[a]	20	86	93
SSM_{Theia}	R	0.28	0.32	0.33
	RMSE (m^3/m^3)	0.1	0.11	0.1
	Bias (m^3/m^3)	0.03	0.04	0.05
	N	20	68	83
$SSM_{SMAP20m}$	R	0.08	0.31	0.08
	RMSE (m^3/m^3)	0.12	0.12	0.13
	Bias (m^3/m^3)	0.08	0.07	0.09
	N	88	222	269

[a] N is the number of data points available for each NDVI range.

(between 0.05 and 0.1 m^3/m^3) because the high SSM values following an irrigation event are not captured by this product. Overall, underestimations are also observed for SSM_{Theia} (biases between 0 and 0.1 m^3/m^3), while SSM_{ρ}, exhibits either positive or negative bias values of approximately 0.05 m^3/m^3. SSM_{ρ} displays RMSE values lower than those for SSM_{Theia} and $SSM_{SMAP20m}$ for 80% of the fields. In particular, 80% of the fields had RMSEs lower than 0.10 m^3/m^3 using SSM_{ρ}, while 36% had RMSEs lower than 0.10 m^3/m^3 using SSM_{Theia}, and only 27% had RMSEs lower than 0.10 m^3/m^3 using $SSM_{SMAP20m}$. Interestingly, a greater difference in performance between the Sentinel-1 products and $SSM_{SMAP20m}$ is observed for summer crops when the number of irrigation events is the higher. For some winter fields, which are mainly irrigated using the sprinkler technique, the Sentinel-1 products exhibit limited performance (for instance, P1 and P3), and $SSM_{SMAP20m}$ outperforms the Sentinel-1 products over these two winter fields, with correlation coefficients between 0.7 and 0.8. Note that the number of $SSM_{SMAP20m}$ points in these fields is low because of several cloudy Sentinel-2 and 3 images.

3.2. Time series analysis

Fig. 5 illustrates some examples of SSM time series from *Prat De Boldu*. Fig. 5a, c and e are summer fields with SSM products available for the entire monitored period. As reported in Table 1, the summer crops cultivated in the study area are usually maize. Examples of winter fields are illustrated in Fig. 5b and d, while Fig. 5f shows the results for the apple orchard that was monitored during winter and summer (from March 31 to October 1, 2021).

For the three summer fields, in situ measurements revealed high SSM variations across the season, mainly in response to frequent irrigation events. As already observed in Fig. 3, the SSM_{ρ} approach retrieves a wide range of SSM values and is in line with the measurement dynamics, while SSM_{Theia} retrievals are always below 0.3 m^3/m^3. The revisit time of $SSM_{SMAP20m}$ is greater than that of the Sentinel-1 products, but the SSM values do not exceed 0.25 m^3/m^3 for most of the time series. For instance, from August 8 to September 28, when almost no rainfall was recorded (see P9 and P11 in Fig. 5), $SSM_{SMAP20m}$ was not able to capture the increases in SSM in response to irrigation events. In contrast, the high values of approximately 0.3 m^3/m^3 that are reported in Fig. 3 can be easily identified in the time series. Interestingly, these values are reported for all the summer fields on approximately June 20 (cf. Fig. 5a, c, e and f). This is most likely related to a rainfall event that wetted the whole study area homogeneously. Consequently, this event is captured by the original coarse pixel of SMAP (and possibly by the 1 km resolution Sentinel-3 pixels), and the information is transferred to the disaggregated product. In contrast, irrigation events occurring at the field scale likely have limited impacts both on the coarse SSM product and on the Sentinel-3 LST used in the disaggregation process.

Fig. 5b and d display the time series for two fields cropped in winter (P2 and P3). As already discussed in the previous section, the data availability of $SSM_{SMAP20m}$ is limited by clouds that can persist in winter in the study region. Indeed, $SSM_{SMAP20m}$ data are lacking over a long

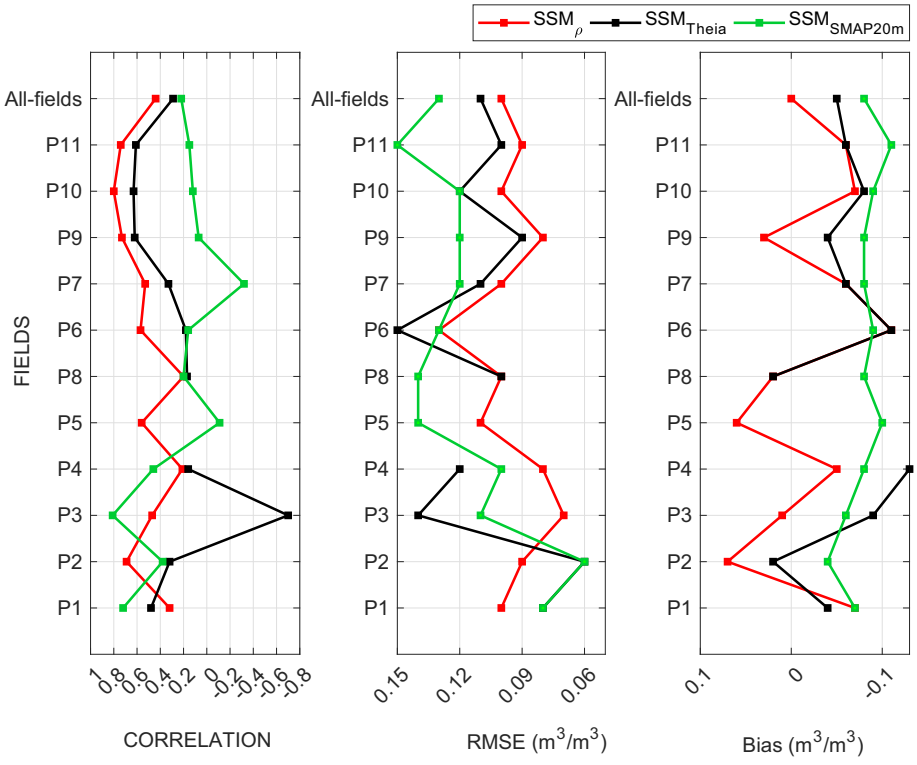

Fig. 4. Correlation coefficients, root mean square errors (RMSE) and biases obtained between in situ measurements and surface soil moisture products by field at *Prat De Boldu*.

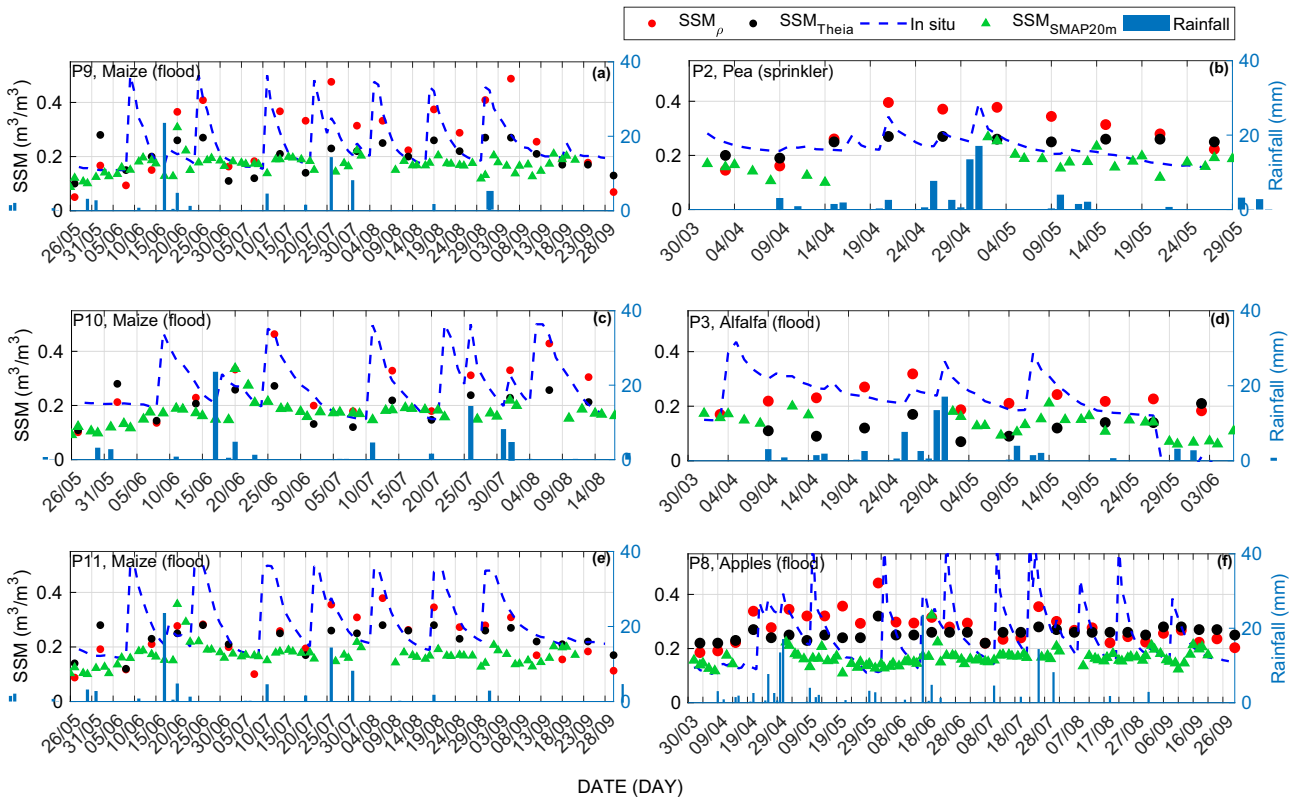

Fig. 5. Time series of SSM_ρ, SSM_{Theia} and $SSM_{SMAP20m}$ surface soil moisture products and in situ measurements over 6 fields at the *Prat De Boldu* site.

period extending from April 14 to May 2. For P2, for instance, most of the irrigation occurred during the latter period, while the dynamics of SSM during the second part of the season, when the product was available, were dominated by rainfall. Consequently, the overall metrics of $SSM_{SMAP20m}$ in this field are reasonable. In addition, for P3 (Fig. 5d), which was cropped with alfalfa, a strong irrigation event at the start of the season around April 4 was missed by the three products because it fell between two Sentinel-1 acquisition times for the Sentinel-1-based products, while the ability to capture localized wetting events such as irrigation at the field scale by $SSM_{SMAP20m}$ was limited, as already highlighted. Finally, although outside of their validity domain, particularly for the Sentinel-1-derived products that were calibrated and validated on annual crops, SSM time series are displayed for an apple orchard in Fig. 4f. Even if the SSM increase at the start of the season around April 19 is properly captured by the satellite-derived products, the three products provide, as expected, poor performance in this field with a very limited dynamic compared to the observations.

3.3. Spatial distribution of SSM

Figs. 6 and 7 display SSM maps over the study area that are derived from the satellite products. The airborne SSM_{GLORI} and Sentinel-2 NDVI maps are also shown for comparison purposes. The closest available dates of Sentinel-1 and SMAP to GLORI acquisition are chosen. Fig. 6 is for July 20, and Fig. 7 is for July 27. All the maps are aggregated to 100-m resolution for comparison with SSM_{GLORI}. Buildings and areas with no data are masked with red and white colors, respectively. Because of the cloud cover, $SSM_{SMAP20m}$ in Fig. 7 is not exploitable. The no data (white spots) for the SSM_{Theia} product is due to low soil contribution for densely vegetated areas that prevent SSM retrieval, while for $SSM_{SMAP20m}$, it is due to cloud cover.

The NDVI map in Fig. 6 illustrates the strong contrast between the irrigated area in the west/northwest region and the non-irrigated part in the east/southeast region. The Sentinel-1-derived products and $SSM_{SMAP20m}$ show contrasting spatial SSM patterns. While SSM_ρ and SSM_{Theia} exhibit similar spatial distributions, with the irrigated area composed of a mosaic of wet and dry fields in relation to contrasting irrigation conditions, $SSM_{SMAP20m}$ displays more homogeneous patterns that are similar to the NDVI map, illustrating that the main downscaling information is related to the auxiliary disaggregation variables. SSM_{GLORI}, whose acquisition time is between one and two days after the satellite products overpass, also exhibits a large range of SSM values in the irrigated area, from almost 0.0 m^3/m^3 to 0.52 m^3/m^3. For the first date (Fig. 6), SSM_{GLORI} displays slightly lower values than the Sentinel-1 products, probably due to the two-day difference between the acquisition times of the products and SSM_{GLORI} maps that can lead to a drying of the soil surface in response to the high temperatures encountered at this time (approximately 35 °C; Zribi et al. (2022)). The SSM_{GLORI} shown in Fig. 6 is, however, characterized by a low moisture level, which is in agreement with the findings of Zribi et al. (2022), who reported that 32% of the pixel values are lower than 0.1 m^3/m^3. The second date (Fig. 7) is characterized by higher SSM level for the Sentinel-1-derived products as well as for SSM_{GLORI}, most likely as a result of an important irrigation event rather than rainfall given the remaining contrasting hydric conditions between the irrigated and non-irrigated areas. Fig. A1 in the appendix displays the spatial variability of the hourly accumulated rainfall maps that were provided by CNRM/Meteo-France using radar and rain gauge data (provided by the Meteorological Service of Catalonia) and made available within the framework of the HILIAISE project (https://www.aeris-data.fr/). These rainfall maps show that at the time of the satellite overpass around 06 h, it has rained almost everywhere, meaning that the spatial variability in SSM cannot be explained by rainfall. In Fig. 7, the saturation around 0.3 m^3/m^3 of the SSM_{Theia} product smooths the SSM spatial pattern by contrast with the SSM_ρ maps, which show significant variations between fields in the range of 0.3–0.5 m^3/m^3 that corresponding to approximately 25% of the SSM_ρ product pixels. Likewise, the SSM_{GLORI} map for the second date also shows that >50% of the pixels are >0.3 m^3/m^3. For SSM_{Theia}, there

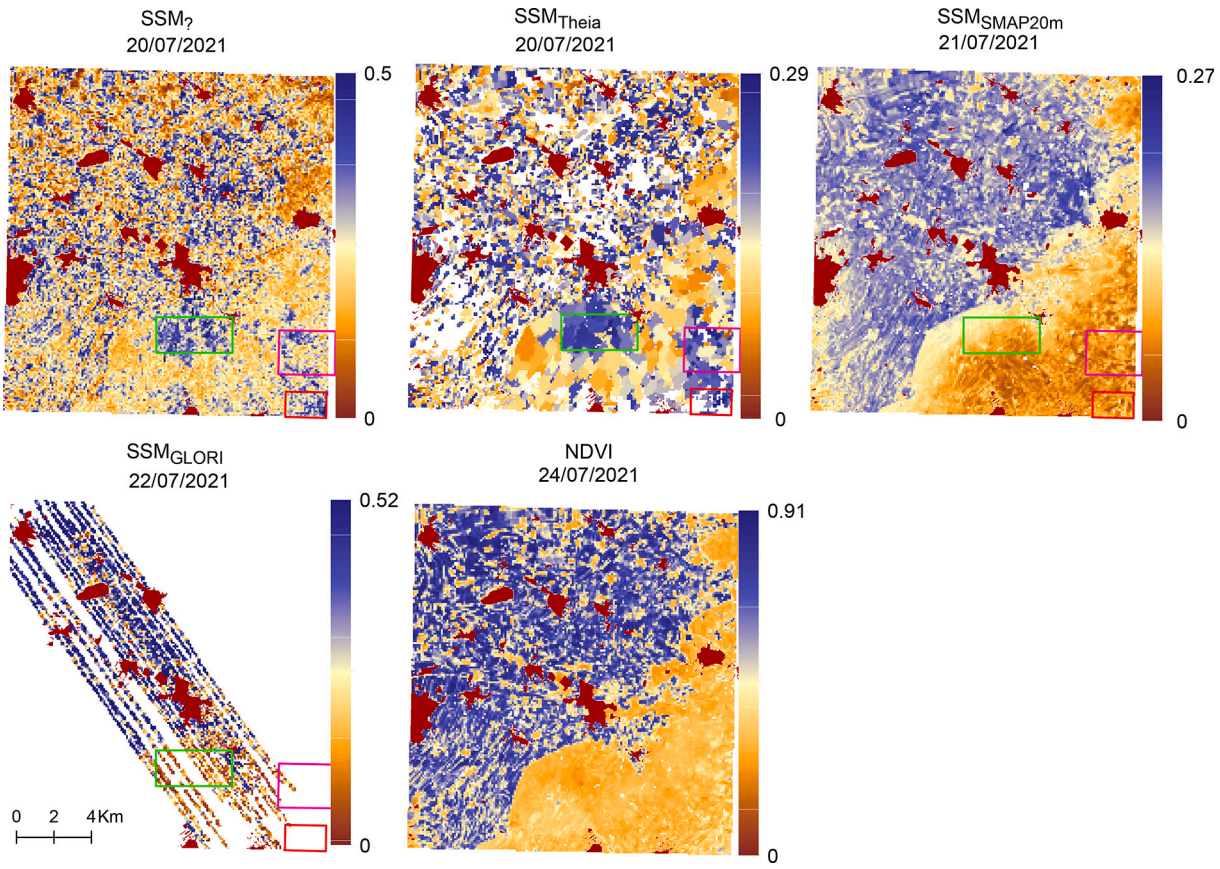

Fig. 6. Surface soil moisture maps over the study area from SSM_{ρ}, SSM_{Theia}, $SSM_{SMAP20m}$ and SSM_{GLORI} at the closest dates to the GLORI acquisition date on July 22. The NDVI is also displayed to support the analysis. The red areas within the maps are buildings (and water surfaces), and the white areas correspond to no data. The three boxes correspond to specific areas discussed in the text. (For interpretation of the references to colour in this figure legend, the reader is referred to the web version of this article.)

was a significant increase between the two dates, with a 41% increase in the number of pixels with an SSM >0.2 m^3/m^3, 65% of which were between 0.25 m^3/m^3 and 0.3 m^3/m^3. The specific spatial pattern of the $SSM_{SMAP20m}$ map for July 27 (Fig. 7) is related to the spatial variability of the Sentinel-3 LST map (showing a cool/mild spot to the south and hotter pixels to the north). Note that the LST image is contaminated by clouds that correspond to the masked pixels on the $SSM_{SMAP20m}$ maps. Interestingly, there are some wet pixels on the Sentinel-1 and SSM_{GLORI} maps that are located southeast of the study region, while those fields are assumed to be rainfed (the three squares in the SSM_{ρ} map in Fig. 6, discussed in the next section). In particular, similar values of approximately 0.3 m^3/m^3 are observed for the SSM_{Theia} and SSM_{ρ} products (Fig. 7) and, to a lesser extent, for the SSM_{GLORI} map that was acquired one day after the Sentinel-1 time overpass. This is discussed later in the manuscript.

4. Discussion

4.1. SSM products: limitations and key areas for improvement

4.1.1. Sentinel-1 products: SSM_{Theia} and SSM_{ρ}

On average, Sentinel-1-derived products outperform the disaggregated $SSM_{SMAP20m}$ and SSM_{ρ} product yields slightly better estimation compared to SSM_{Theia}. It is however important to highlight that the SSM_{ρ} method was improved to the specific characteristics of the fields in the study area by broadening the range of the soil roughness variable h_{rms} in line with the smoother field encountered in the region. By contrast, SSM_{Theia} product was assessed without any adaptation of the retrieval method. The results of this study showed that SSM_{Theia} product suffers from saturation of retrieved values above 0.3 m^3/m^3 for fields with high SSM, while the C-band signal is sensitive to SSM variations of up to 0.5 m^3/m^3 (Hoskera et al., 2020; Huang et al., 2019; Zheng et al., 2021). It was checked that it could not be attributed to a poor calibration of the soil moisture sensors by rescaling the in situ data to the range of SSM_{Theia} products with no improvement in the statistical metrics. This saturation is not related to the range of the dataset used to train the algorithm (Qu et al., 2021) since the training sets range from 0.05 to 0.45 m^3/m^3 (El Hajj et al., 2017). During the training phase of the neural network that was designed to estimate SSM_{Theia}, minimization of the difference between reference values and estimated values (zero overall bias for data with SSM between 0.04 m^3/m^3 and 0.4 m^3/m^3) is achieved, with a slight overestimation of the SSM for reference SSM smaller than 0.25 m^3/m^3 and an underestimation of the SSM for reference SSM between 0.25 m^3/m^3 and 0.40 m^3/m^3. The saturation problem that is observed for high SSM values is therefore mainly due to a saturation of the used soil backscattering model MIEM. In addition, the angle of incidence of Sentinel-1 (between 30° and 45°), which is not always optimal for estimating SSM, amplifies this saturation problem.

On average, even if the Sentinel-1-derived products provide acceptable statistical metrics, the values of the metrics, including RMSE, are obviously higher than the errors reported on the site where the methods were developed. Indeed, both Sentinel-1 approaches were calibrated and validated on annual crops composed mainly of wheat fields while the database in this study is more diversified in terms of crops (e.g., pea, alfalfa, barley, wheat, and maize) and agricultural practices (e.g., sown variety, and soil practices). Both Sentinel-1-derived approaches rely on the calibration of the WCM, which was carried out mainly on wheat crops in semi-arid regions (see El Hajj et al. (2017) for

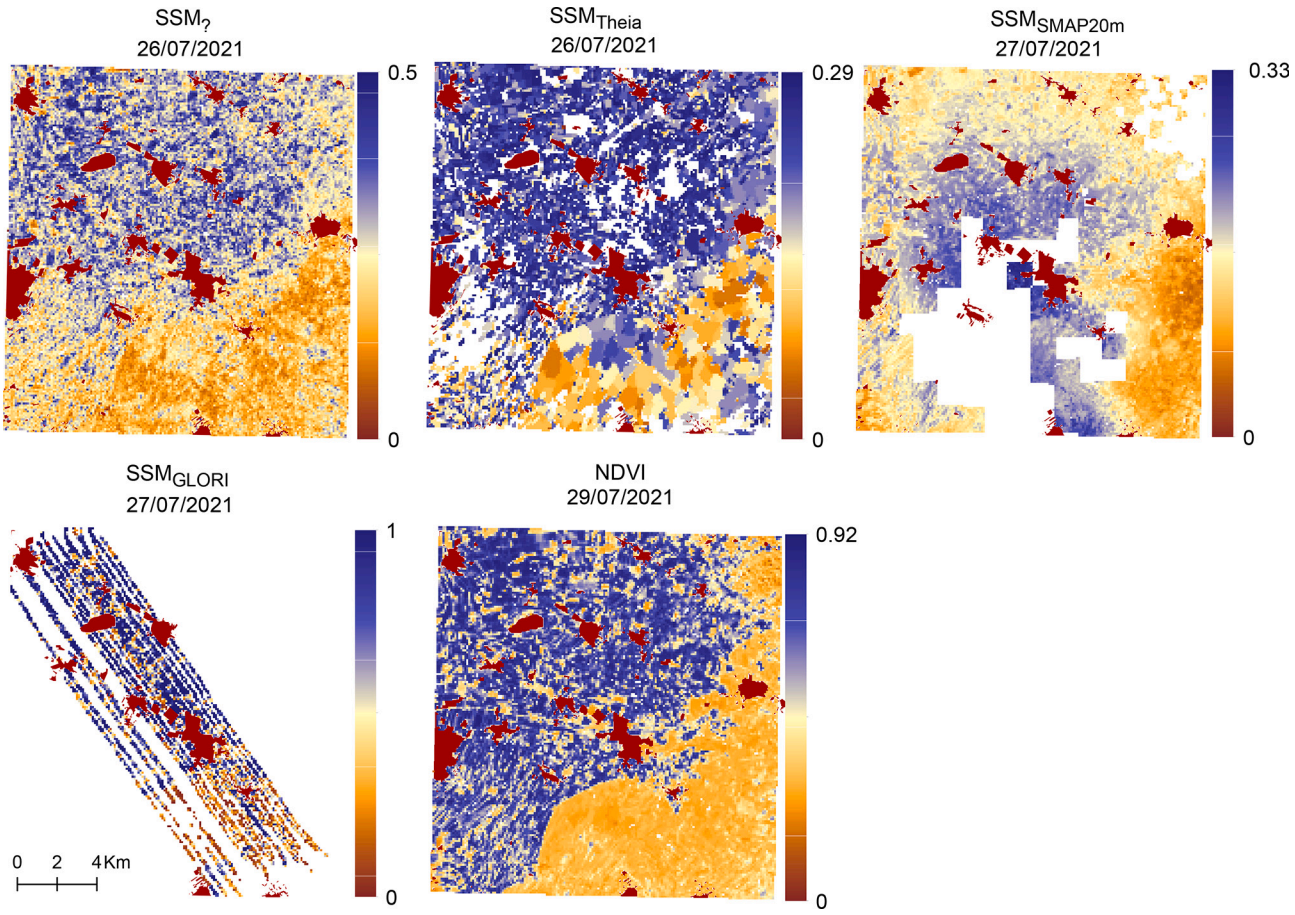

Fig. 7. Surface soil moisture maps over the study area from SSM_{ρ}, SSM_{Theia}, $SSM_{SMAP20m}$ and SSM_{GLORI} at the closest dates to the GLORI acquisition date on July 27. The NDVI is also displayed to support the analysis. The red areas within the maps are buildings (and water surfaces), and the white areas correspond to no data. (For interpretation of the references to colour in this figure legend, the reader is referred to the web version of this article.)

SSM_{Theia} and Ouaadi et al. (2020) for SSM_{ρ}). They offered reasonable results for other annuals with similar canopy structures, including the leaf angle distributions close to those of erectophile plants, such as barley, but also providing acceptable performance for maize with a different geometry (row crop and leaf angle distributions closer to the planophile). For the Sentinel-1-derived products, this different geometry would most likely impact the calibration of the two parameters that are related to the canopy structure in the WCM (parameters A and B; Attema and Ulaby, 1978). A specific calibration for maize would probably improve the retrieval accuracy. This acceptable performance for maize could be due to the "optimal" climatic conditions that could mask the effect of canopy geometry. Indeed, maize was cropped in summer, which offers the best conditions for soil moisture retrieval, as a strong contrast in terms of the SSM can be observed from the very dry upper surface before an irrigation event and very wet conditions immediately after. In agreement with this assumption, a lower performance of the Sentinel-1 products was observed for some winter crops than for summer crops. In addition to the climatic conditions being more favorable in summer, dew and water interception, which are more likely to occur in winter, were found to impact the backscattering signal (Khabbazan et al., 2022; Riedel et al., 2002), leading to errors in SSM estimations (Hornbuckle et al., 2010; Kasischke et al., 2009; Mladenova et al., 2011), as they are not accounted for by backscattering models. Poor results are also observed for trees for the three satellite products. Indeed, trees are characterized by a more complex geometry than annuals and are composed of an underlying layer of trunks and an upper layer containing crowns with branches and leaves. In addition, it is probable that adopting a more complex multilayer model than the simple WCM such as Karam (Karam et al., 1992) and MIMICS (Ulaby et al., 1990) would better represent the contributions of the different canopy layers and canopy attenuation and thus could contribute to improving SSM retrievals. Nevertheless, such a more realistic representation of the canopy would require further variables and parameters characterizing the different scatterers of trees (trunk, branch and leaf geometrical and dielectric characteristics) that would be difficult to prescribe for large areas.

4.1.2. *Disaggregated product:* $SSM_{SMAP20m}$

$SSM_{SMAP20m}$ has a high temporal resolution with respect to the Sentinel-1-derived products, but its ability to detect irrigation signals is limited. Given the good results obtained over parts of the season when the SSM dynamics are low and/or are dominated by rainfall events, $SSM_{SMAP20m}$, in its actual state of development, would be well suited for SSM monitoring over rainfed areas. Indeed, DisPATCH preserves the information from the original microwave product (Qu et al., 2021), meaning that rainfall events are captured by the disaggregated approach because they impact the whole coarse-scale pixel. In contrast, irrigation events that occur at the field scale are not captured by the coarse pixel that also encompasses the surrounding dry fields (Escorihuela and Quintana-Seguí, 2016; Fontanet et al., 2018; Mladenova et al., 2011). Consequently, irrigation events are detected only if the very high-resolution variable used within the disaggregation process is related to the hydric status. Indeed, $SSM_{SMAP20m}$ used Sentinel-3 thermal data (LST) that are a good representative of the surface hydric status when water is a limiting factor (Long et al., 2019). Unfortunately, due to the lack of frequent revisit time and very high spatial resolution thermal

data from the sensors currently in orbit, the Sentinel-2 reflectances are used as proxy information for the 20-m SSM product (via downscaling Sentinel-3 LST) but this information is not related to the hydric status of the land surface. This means that for a heterogeneous irrigated area in a semiarid region, such as our study area, where the SSM are dominated by localized irrigation events, the water content of the upper soil surface can be locally high immediately after an irrigation event, while two days later, the upper soil profile could be completely dry. These contrasting conditions cannot be represented by $SSM_{SMAP20m}$. This was also observed by Qu et al. (2021), who reported that disaggregated SSM products were not able to capture rapid temporal changes in SSM. In addition, disaggregated approaches are generally associated with uncertainties due to downscaling and spatial heterogeneity (Al-Yaari et al., 2019; Draper et al., 2009). Similarly, this trend was also observed for the SSM spatial patterns on two dates in July 2021. Indeed, the spatial patterns of the $SSM_{SMAP20m}$ product are similar to those of the NDVI and LST maps. This finding is in line with several studies that have pointed out that the spatial patterns of the disaggregated products are closely related to the spatial patterns of the auxiliary variables used in the downscaling process (Gruber et al., 2020; Peng et al., 2017; Qu et al., 2021). Interestingly, the future launch of thermal sensors that combine very high-resolution and frequent revisit time such as TRISHNA and LSTM, will offer interesting opportunities to improve SSM products based on microwave brightness temperatures, such as the $SSM_{SMAP20m}$ product, or future products that could be derived from SMOS and SMAP data.

4.2. Irrigation occurrence and subsurface scattering effect

In contrast to $SSM_{SMAP20m}$, both Sentinel-1 products depict large areas with high SSM values in regions that are known to be non-irrigated. This is also observed by the airborne GLORI GNSS-R instrument. To investigate this specific point, Fig. 8 displays images from Google Earth Pro that were acquired in August 2021 and show three sample zones (see Fig. 6) in the non-irrigated area. Fig. 8 demonstrates that apart from some fields that could be cropped and thus irrigated during this summer period (in particular those close to the Segarra-Garrigues irrigation canal; see Zone 2 and Zone 3 in Fig. 8), most of the area is composed of dryland crops (see the classification of irrigated fields in https://agricultura.gencat.cat/ca/ambits/desenvolupament-rural/sigpac/mapa-cultius/). In fact, 70.000 ha of non-irrigated land in these regions were intended to be converted into irrigated land through the Segarra-Garrigues canal as part of a European project since the 2000s (Cerrillo, 2015). Although most of the area has not been converted to irrigation because of ecological considerations (the area is

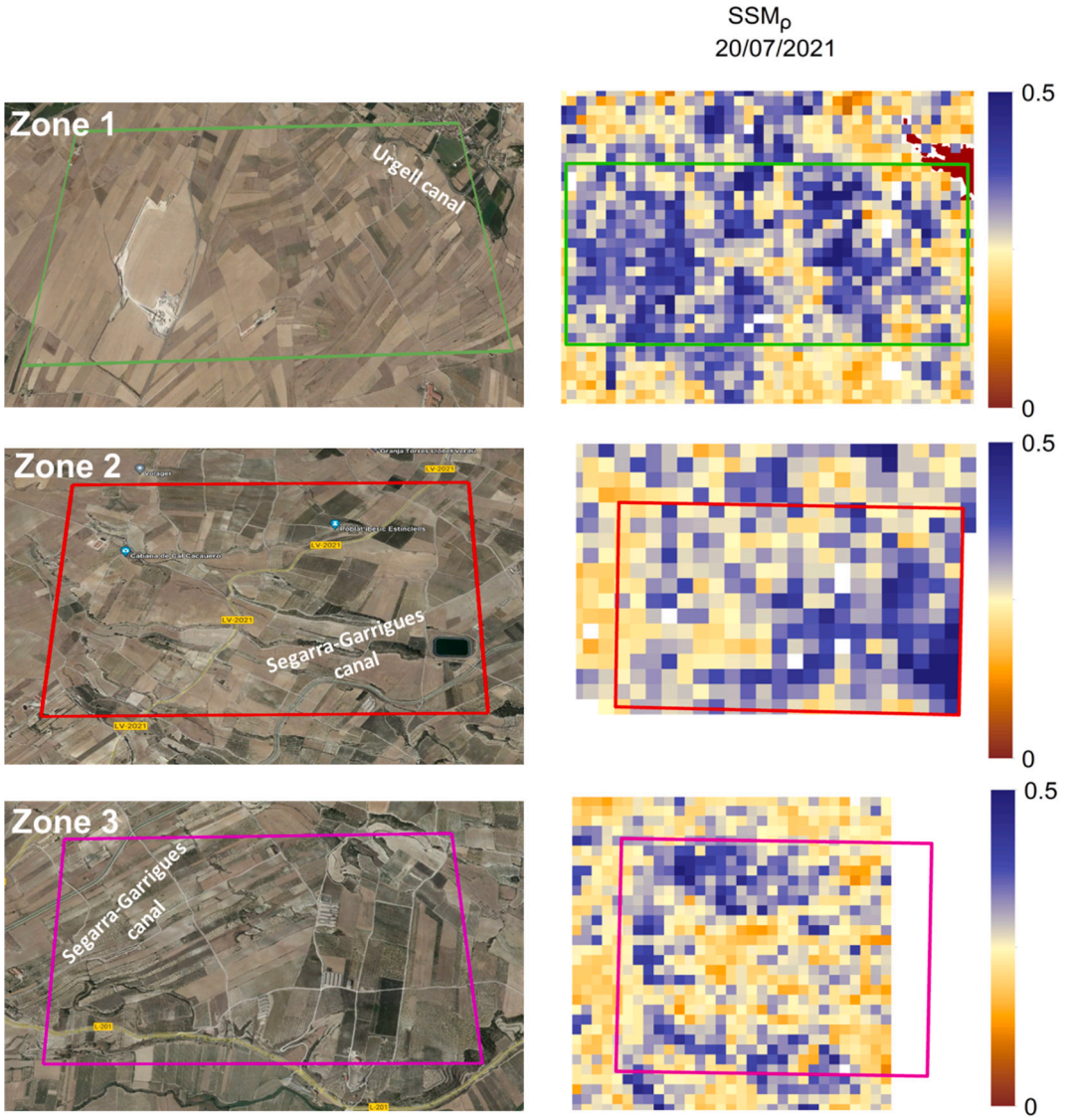

Fig. 8. The three enlargements of the non-irrigated areas (see Fig. 6) from Google Earth Pro (images acquired in August 2021) and the SSM_{ρ} map of July 20.

classified as a special protection area (SPA) of Natura 2000, an EU-wide nature protection network; Rojas-Briales (2000)), 11% of this area has already adhered to the irrigation system (Cerrillo, 2015). While the region is dryland, large areas with high SSM values are observed on the Sentinel-1 products (see, for instance, Zone 1 for SSM_ρ in Fig. 8). The first explanation for these high SSM values could be related to subsurface scattering that can occur for very dry soils in response to bedrock located under the soil surface or in response to distributed rocks and stones along the soil's vertical profile. The microwaves penetrate the soil and interact with the underground components, leading to a high level of backscattering. This has already been reported for the C-band by various authors (Escorihuela and Quintana-Seguí, 2016; Morrison and Wagner, 2020; Wagner et al., 2022) over several regions including our study region. In this study, the penetration depth at the C-band is computed for the loam and silt-loam soils in the regions where subsurface scattering could occur (Zone 1 in Fig. 8). The penetration depth of microwave wavelengths in the soil can be computed using the formula of Ulaby et al. (1984):

$$\delta_p = \frac{\lambda}{4\pi}\left(\frac{\epsilon'}{2}\left(\left(1+\left(\frac{\epsilon''}{\epsilon'}\right)^2\right)^{0.5}-1\right)\right)^{-0.5} \quad (1)$$

where λ is the wavelength and ϵ' and ϵ'' are the real and imaginary parts, respectively, of the dielectric constant ϵ of the soil. ϵ is computed from the SSM and soil texture using the empirical model proposed in Hallikainen et al. (1985). Table A1 in the appendix summarizes the results for the boundary of the loam and silt-loam soil classes in the C-band ($\lambda = 6$ cm). As expected, the penetration of C-band wave is deeper under dry soil conditions and can reach up to 17.6 cm for SSM = 0.04 m^3/m^3. On the SSM maps of July 20 and 26, the moistening caused by the precipitation occurred on July 26 (Fig. A1 in the appendix) is clear for the irrigated area while a slight trend to drying between the two dates is strangely observed on the non-irrigated region. This could support the assumption of subsurface scattering occurrence, as the increase in SSM associated with rainfall may have reduced the penetration depth and thus the subsurface scattering contribution to the backscattered signal. Nevertheless, the high SSM spots in Zone 1 on the Sentinel-1 SSM products are not observed at the L-band with the GLORI instrument (except for some wet pixels on the right side of Zone 1). This could be explained by the deeper penetration of the L-band compared to the C-band (20 cm for SSM = 0.04 m^3/m^3 for instance). In addition, the roughness of the subsurface is relative to the wavelength, so the size of the scatterers is small for the L-band and consequently the contribution from the subsurface is lower for the L-band than for the C-band. The second possible explanation is the presence of irrigated fields in this area (Zone 1) that could have dried up as the GLORI flights were carried out one or two days after the Sentinel-1 overpass, considering the extreme temperature encountered in the region in July. Finally, an underestimation of the retrieved h_{rms} by the retrieval algorithms of SSM_ρ and, to a lesser extent, SSM_{Theia} could also cause the retrieval of high SSM values: the algorithm would compensate a low roughness by high SSM values to explain the observed backscattered signal. Nevertheless, an underestimation of soil roughness is an assumption that is not favored as (1) smooth fields are observed during field visits on Zone 1 and (2) SSM_{Theia}, based on a different retrieval algorithm also displays high values of SSM.

5. Conclusion

The aim of the present study was to perform, for the first time, an intercomparison study of high spatial resolution SSM products derived from satellite observations. Three products were compared and evaluated using a large database of in situ SSM data that were collected in the Ebro Basin (Catalonia, Spain). The results show that SSM_ρ provides better metrics than SSM_{Theia} and $SSM_{SMAP20m}$, with correlation coefficients $R > 0.4$ for 72%, 40% and 27% of the fields for SSM_ρ, SSM_{Theia} and $SSM_{SMAP20m}$, respectively. The lower performance of SSM_{Theia} and $SSM_{SMAP20m}$ is mainly related to (i) a saturation of SSM_{Theia} at approximately 0.3 m^3/m^3 because of the saturation of the soil backscattering model for SSM values above 0.3 m^3/m^3 and (ii) the insensitivity of $SSM_{SMAP20m}$ to SSM variations in response to irrigation. Indeed, the Sentinel-2 reflectances used within the disaggregation process are not related to the surface hydric status. The main conclusions that aimed at improving the current high-resolution mapping of the SSM approaches can be summarized as follows:

(1) The methods based on Sentinel-1 data need improvement for tree canopies, as the two approaches were calibrated on cereals and validated on annual crops. Multilayer backscattering models should be considered to provide a better representation of canopy scatterer groups (e.g., leaves, branches and trunks) and their contributions and interactions.
(2) The saturation of the SSM_{Theia} is the main limit of this approach, and the use of a soil backscattering model allowing a wider range of SSM variations could improve the retrievals. The calibration of WCM coefficients for SSM_{Theia} and SSM_ρ for each crop type and/or different farming practices, instead of using constant coefficients that have been calibrated mainly for wheat crops, could also improve the estimations.
(3) The use of high spatiotemporal resolution thermal data that will be available with future TRISHNA and LSTM missions instead of optical data will probably improve the methods based on the disaggregation of SSM derived from coarse-scale microwave radiometer data, such as $SSM_{SMAP20m}$.

It is important, however, to stress the need for further intercomparison studies that cover other regions, including additional data and, notably, other products. Indeed, with future missions that involve domains with different wavelengths, new SSM products will be available, and important improvements in the available approaches are expected. This should obviously be accompanied by extensive and extended in situ measurement campaigns on contrasting eco-agro-systems. Indeed, intercomparison studies should cover not only crops but also natural vegetation, which are vital for local and global studies such as carbon balance, wildfires and drought monitoring.

Finally, the penetration depth of the C-band signal within canopies is low and limits the contribution of the ground to the total backscattered signal (Das and Kumar, 2015; Ulaby et al., 1996; Wang et al., 2018). This highlights the potential added value of future missions using low frequencies, such as the L-band NISAR (NISAR, 2019), which will be launched in 2024. Indeed, the L-band was found to be less sensitive to dense vegetation cover than the C-band and provides an important contribution from the soil because of its greater penetration ability (Das and Kumar, 2015; Wang et al., 2000). The combination of the C- and L-bands could lead to better characterizations of soil and vegetation contributions for a more accurate estimations of SSM with good spatiotemporal resolution, particularly with the future ESA Sentinel-1 NG (for New Generation) C-band mission with a revisit time objective of 4 days and resolution of 5 m (Mariantonietta Zonno et al., 2021).

CRediT authorship contribution statement

Nadia Ouaadi: Writing – review & editing, Writing – original draft, Visualization, Methodology, Investigation, Formal analysis, Data curation, Conceptualization. **Lionel Jarlan:** Writing – review & editing, Writing – original draft, Investigation, Funding acquisition, Formal analysis, Conceptualization. **Michel Le Page:** Writing – review & editing, Formal analysis, Data curation. **Mehrez Zribi:** Writing – review & editing, Data curation. **Giovani Paolini:** Writing – review & editing, Formal analysis, Data curation. **Bouchra Ait Hssaine:** Writing – review & editing, Formal analysis. **Maria Jose Escorihuela:** Writing – review & editing, Formal analysis. **Pascal Fanise:** Writing – review & editing,

Data curation. **Olivier Merlin:** Writing – review & editing, Formal analysis. **Nicolas Baghdadi:** Writing – review & editing, Formal analysis, Data curation. **Aaron Boone:** Writing – review & editing, Funding acquisition, Formal analysis.

Declaration of competing interest

The authors declare that they have no known competing financial interests or personal relationships that could have appeared to influence the work reported in this paper.

Data availability

Data will be made available on request.

Acknowledgments

This study was conducted as part of the ANR-19-CE01-0017 HILIAISE project, in which N.O. has been funded. The authors are thankful for the financial support of the Rise-H2020-ACCWA project. The authors would like to thank Dr. Pierre-Louis Frison for the insightful discussions, and Dr. Josep Ramon Miró Cubells for providing the rainfall maps.

Appendix

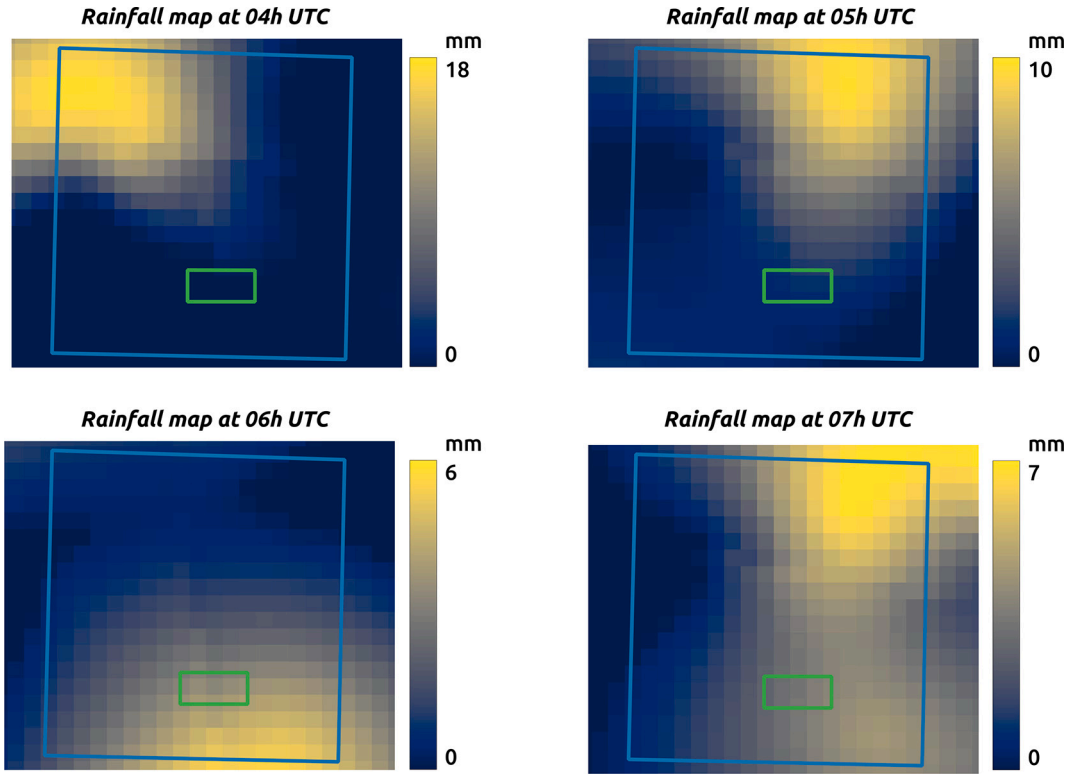

Fig. A1. Hourly rainfall maps between 04 h and 07 h on 26 July over the study area (blue box). The green box is Zone 1 (Fig. 8). (For interpretation of the references to colour in this figure legend, the reader is referred to the web version of this article.)

Table A1
Penetration depths at the C-band computed for loam and silt-loam class boundaries (obtained from the triangular diagram of soil texture) for two SSM levels.

		Soil composition		Penetration depth (cm)	
		Sand	Clay	for SSM = 0.04 m^3/m^3	for SSM = 0.1 m^3/m^3
Loam	Soil 1	52.5	20	13.213	3.341
	Soil 2	22.5	27.5	15.889	3.582
	Soil 3	42.5	7.5	12.828	3.291
	Soil 4	52.5	7.5	12.344	3.243
	Soil 5	45	27.5	14.261	3.448
Silt-Loam	Soil 1	50	0	11.990	3.198
	Soil 2	22.5	27.5	15.802	3.582
	Soil 3	0	27.5	17.670	3.724
	Soil 4	0	12.5	15.823	3.561
	Soil 5	7.5	12.5	15.292	3.518
	Soil 6	20	0	13.443	3.340

References

Ahlström, A., Raupach, M.R., Schurgers, G., Smith, B., Arneth, A., Jung, M., Reichstein, M., Canadell, J.G., Friedlingstein, P., Jain, A.K., Kato, E., Poulter, B., Sitch, S., Stocker, B.D., Viovy, N., Wang, Y.P., Wiltshire, A., Zaehle, S., Zeng, N., 2015. The dominant role of semi-arid ecosystems in the trend and variability of the land CO2 sink. Science (80-.) 348, 895–899. https://doi.org/10.1002/2015JA021022.

Ait Hssaine, B., Merlin, O., Rafi, Z., Ezzahar, J., Jarlan, L., Khabba, S., Er-raki, S., 2018. Calibrating an evapotranspiration model using radiometric surface temperature, vegetation cover fraction and near-surface soil moisture data. Agric. For. Meteorol. 257, 104–115. https://doi.org/10.1016/j.agrformet.2018.02.033.

Ait Hssaine, B., Chehbouni, A., Er-raki, S., Khabba, S., Ezzahar, J., Ouaadi, N., Ojha, N., Rivalland, V., Merlin, O., 2021. On the utility of high-resolution soil moisture data for better constraining thermal-based energy balance over three semi-arid agricultural areas. Remote Sens. 13, 727. https://doi.org/10.3390/rs13040727.

Al-Yaari, A., Wigneron, J.P., Dorigo, W., Colliander, A., Pellarin, T., Hahn, S., Mialon, A., Richaume, P., Fernandez-Moran, R., Fan, L., Kerr, Y.H., De Lannoy, G., 2019. Assessment and inter-comparison of recently developed/reprocessed microwave satellite soil moisture products using ISMN ground-based measurements. Remote Sens. Environ. 224, 289–303. https://doi.org/10.1016/j.rse.2019.02.008.

Ameur, F., Amichi, H., Leauthaud, C., 2020. Agroecology in North African irrigated plains ? Mapping promising practices and characterizing farmers ' underlying logics. Reg. Environ. Chang. 20, 133. https://doi.org/10.1007/s10113-020-01719-1.

Arias, M., Campo-Bescos, M.A., Arregui, L.M., Gonzalez-Audicana, M., Alvarez-Mozos, J., 2022. A New Methodology for Wheat Attenuation Correction at C-Band VV-Polarized Backscatter Time Series. IEEE Trans. Geosci. Remote Sens. 60 https://doi.org/10.1109/TGRS.2022.3176144.

Attema, E.P.W., Ulaby, F.T., 1978. Vegetation modeled as a water cloud. Radio Sci. 13, 357–364. https://doi.org/10.1029/RS013i002p00357.

Baghdadi, N., Abou Chaaya, J., Zribi, M., 2011. Semiempirical calibration of the integral equation model for SAR data in C-band and cross polarization using radar images and field measurements. IEEE Geosci. Remote Sens. Lett. 8, 14–18. https://doi.org/10.1109/LGRS.2010.2050054.

Bai, X., He, B., Li, X., Zeng, J., Wang, X., Wang, Z., Zeng, Y., Su, Z., 2017. First assessment of sentinel-1A data for surface soil moisture estimations using a coupled water cloud model and advanced integral equation model over the Tibetan plateau. Remote Sens. 9, 1–20. https://doi.org/10.3390/rs9070714.

Bao, Y., Zhang, Y., Wang, J., Min, J., 2014. Surface soil moisture estimation over dense crop using Envisat ASAR and Landsat TM imagery: an approach. Int. J. Remote Sens. 35, 6190–6212. https://doi.org/10.1080/01431161.2014.951098.

Bériaux, E., Waldner, F., Collienne, F., Bogaert, P., Defourny, P., 2015. Maize Leaf Area Index retrieval from synthetic quad pol SAR time series using the water cloud model. Remote Sens. 7, 16204–16225. https://doi.org/10.3390/rs71215818.

Bouras, E. houssaine, Olsson, P.O., Thapa, S., Díaz, J.M., Albertsson, J., Eklundh, L., 2023. Wheat yield estimation at high spatial resolution through the assimilation of Sentinel-2 data into a crop growth model. Remote Sens. 15 https://doi.org/10.3390/rs15184425.

Brocca, L., Melone, F., Moramarco, T., Morbidelli, R., 2010. Spatial-temporal variability of soil moisture and its estimation across scales. Water Resour. Res. 46, 1–14. https://doi.org/10.1029/2009WR008016.

Brocca, L., Hasenauer, S., Lacava, T., Melone, F., Moramarco, T., Wagner, W., Dorigo, W., Matgen, P., Martínez-Fernández, J., Llorens, P., Latron, J., Martin, C., Bittelli, M., 2011. Soil moisture estimation through ASCAT and AMSR-E sensors: an intercomparison and validation study across Europe. Remote Sens. Environ. 115, 3390–3408. https://doi.org/10.1016/j.rse.2011.08.003.

Cerrillo, A., 2015. Los ocho naufragios del canal Segarra-Garrigues [WWW Document]. Lavanguardia (natural). URL. https://www.lavanguardia.com/natural/20151108/54439693500/ocho-naufragios-canal-segarra-garrigues.html.

Chan, S.K., Bindlish, R., O'Neill, P., Jackson, T., Njoku, E., Dunbar, S., Chaubell, J., Piepmeier, J., Yueh, S., Entekhabi, D., Colliander, A., Chen, F., Cosh, M.H., Caldwell, T., Walker, J., Berg, A., McNairn, H., Thibeault, M., Martínez-Fernández, J., Uldall, F., Seyfried, M., Bosch, D., Starks, P., Holifield Collins, C., Prueger, J., van der Velde, R., Asanuma, J., Palecki, M., Small, E.E., Zreda, M., Calvet, J., Crow, W.T., Kerr, Y., 2018. Development and assessment of the SMAP enhanced passive soil moisture product. Remote Sens. Environ. 204, 931–941. https://doi.org/10.1016/j.rse.2017.08.025.

Cheng, Y., 1995. Mean shift, mode seeking, and clustering. IEEE Trans. Pattern Anal. Mach. Intell. 17, 790–799. https://doi.org/10.1109/34.400568.

Choi, M., Hur, Y., 2012. A microwave-optical/infrared disaggregation for improving spatial representation of soil moisture using AMSR-E and MODIS products. Remote Sens. Environ. 124, 259–269. https://doi.org/10.1016/J.RSE.2012.05.009.

Das, K., Kumar, P., 2015. Present status of soil moisture estimation by microwave remote sensing. Cogent Geosci. 1, 1084669. https://doi.org/10.1080/23312041.2015.1084669.

Defourny, P., Bontemps, S., Bellemans, N., Cara, C., Dedieu, G., Guzzonato, E., Hagolle, O., Inglada, J., Nicola, L., Rabaute, T., Savinaud, M., Udroiu, C., Valero, S., Bégué, A., Dejoux, J., El, A., Ezzahar, J., Kussul, N., Labbassi, K., Lebourgeois, V., Miao, Z., Newby, T., Nyamugama, A., Salh, N., Shelestov, A., Simonneaux, V., Sibiry, P., Traore, S.S., Koetz, B., 2019. Near real-time agriculture monitoring at national scale at parcel resolution: performance assessment of the Sen2-Agri automated system in various cropping systems around the world. Remote Sens. Environ. 221, 551–568. https://doi.org/10.1016/j.rse.2018.11.007.

Diarra, A., Jarlan, L., Er-Raki, S., Le Page, M., Aouade, G., Tavernier, A., Boulet, G., Ezzahar, J., Merlin, O., Khabba, S., 2017. Performance of the two-source energy budget (TSEB) model for the monitoring of evapotranspiration over irrigated annual crops in North Africa. Agric. Water Manag. 193 https://doi.org/10.1016/j.agwat.2017.08.007.

Dobermann, A., Witt, C., Abdulrachman, S., Gines, H.C., Nagarajan, R., Son, T.T., Tan, P. S., Wang, G.H., Chien, N.V., Thoa, V.T.K., Phung, C.V., Stalin, P., Muthukrishnan, P., Ravi, V., Babu, M., Simbahan, G.C., Adviento, M.A.A., 2003. Soil fertility and indigenous nutrient supply in irrigated rice domains of Asia. Agron. J. 95, 913–923. https://doi.org/10.2134/agronj2003.9130.

Dobriyal, P., Qureshi, A., Badola, R., Hussain, S.A., 2012. A review of the methods available for estimating soil moisture and its implications for water resource management. J. Hydrol. 458–459, 110–117. https://doi.org/10.1016/j.jhydrol.2012.06.021.

Draper, C.S., Walker, J.P., Steinle, P.J., De Jeu, R.A.M., Holmes, T.R.H., 2009. An evaluation of AMSR – E derived soil moisture over Australia. Remote Sens. Environ. 113, 703–710. https://doi.org/10.1016/j.rse.2008.11.011.

Dubois, P.C., Zyl, J. van, Engman, T., 1995. Measuring soil moisture with imaging radars. IEEE Trans. Geosci. Remote Sens. 33, 915–926. https://doi.org/10.1109/36.406677.

El Hajj, M., Baghdadi, N., Zribi, M., Bazzi, H., 2017. Synergic use of Sentinel-1 and Sentinel-2 images for operational soil moisture mapping at high spatial resolution over agricultural areas. Remote Sens. 9, 1–28. https://doi.org/10.3390/rs9121292.

Entekhabi, B.D., Njoku, E.G., Neill, P.E.O., Kellogg, K.H., Crow, W.T., Edelstein, W.N., Entin, J.K., Goodman, S.D., Jackson, T.J., Johnson, J., Kimball, J., Piepmeier, J.R., Koster, R.D., Martin, N., Mcdonald, K.C., Moghaddam, M., Moran, S., Reichle, R., Shi, J.C., Spencer, M.W., Thurman, S.W., Tsang, L., Van Zyl, J., 2010. TheSoilMoistureActivePassive (SMAP). IEEE Proc. 704–716.

Escorihuela, M.J., Quintana-Seguí, P., 2016. Comparison of remote sensing and simulated soil moisture datasets in Mediterranean landscapes. Remote Sens. Environ. 180, 99–114. https://doi.org/10.1016/j.rse.2016.02.046.

Fontanet, M., Fernàndez-Garcia, D., Ferrer, F., 2018. The value of satellite remote sensing soil moisture data and the DISPATCH algorithm in irrigation fields. Hydrol. Earth Syst. Sci. 22, 5889–5900. https://doi.org/10.5194/hess-22-5889-2018.

Fung, A.K., Zongqian, L., Chen, K.S., 1992. Backscattering from a randomly rough dielectric surface. IEEE Trans. Geosci. Remote Sens. 30, 356–369. https://doi.org/10.1109/36.134085.

GCOS, 2021. The Status of the Global Climate Observing System 2021: The GCOS Status Report (GCOS-240). Switzerland, Geneva.

Gherboudj, I., Magagi, R., Berg, A.A., Toth, B., 2011. Soil moisture retrieval over agricultural fields from multi-polarized and multi-angular RADARSAT-2 SAR data. Remote Sens. Environ. 115, 33–43. https://doi.org/10.1016/j.rse.2010.07.011.

Gokmen, M., Vekerdy, Z., Verhoef, A., Verhoef, W., Batelaan, O., van der Tol, C., 2012. Integration of soil moisture in SEBS for improving evapotranspiration estimation under water stress conditions. Remote Sens. Environ. 121, 261–274. https://doi.org/10.1016/j.rse.2012.02.003.

Greifeneder, F., Notarnicola, C., Hahn, S., Vreugdenhil, M., Reimer, C., Santi, E., Paloscia, S., Wagner, W., 2018. The Added Value of the VH/VV Polarization-Ratio for Global Soil Moisture Estimations from Scatterometer Data. IEEE J. Sel. Top. Appl. Earth Obs. Remote Sens. 11, 3668–3679. https://doi.org/10.1109/JSTARS.2018.2865185.

Gruber, A., De Lannoy, G., Albergel, C., Al-Yaari, A., Brocca, L., Calvet, J.C., Colliander, A., Cosh, M., Crow, W., Dorigo, W., Draper, C., Hirschi, M., Kerr, Y., Konings, A., Lahoz, W., McColl, K., Montzka, C., Muñoz-Sabater, J., Peng, J., Reichle, R., Richaume, P., Rüdiger, C., Scanlon, T., van der Schalie, R., Wigneron, J. P., Wagner, W., 2020. Validation practices for satellite soil moisture retrievals: what are (the) errors? Remote Sens. Environ. 244, 118061 https://doi.org/10.1016/j.rse.2020.111806.

Gruhier, C., De Rosnay, P., Hasenauer, S., Holmes, T., De Jeu, R., Kerr, Y., Mougin, E., Njoku, E., Timouk, F., Wagner, W., Zribi, M., 2010. Soil moisture active and passive microwave products: Intercomparison and evaluation over a Sahelian site. Hydrol. Earth Syst. Sci. 14, 141–156. https://doi.org/10.5194/hess-14-141-2010.

Guzinski, R., Nieto, H., 2019. Evaluating the feasibility of using Sentinel-2 and Sentinel-3 satellites for high-resolution evapotranspiration estimations. Remote Sens. Environ. 221, 157–172. https://doi.org/10.1016/j.rse.2018.11.019.

Hallikainen, M.T., Ulabz, F.T., Dobson, M.C., El-Rayes, M.A., Wu, L.K., 1985. Microwave dielectric behavior of wet soil-part I: empirical models and experimental observations. IEEE Trans. Geosci. Remote Sens. GE-23, 25–34. https://doi.org/10.1109/TGRS.1985.289497.

He, B., Xing, M., Bai, X., 2014. A synergistic methodology for soil moisture estimation in an alpine prairie using radar and optical satellite data. Remote Sens. 6, 10966–10985. https://doi.org/10.3390/rs61110966.

Hornbuckle, B.K., Rowlandson, T.L., Russell, E., Kaleita, A., Logsdon, S., Kruger, A., Yueh, S., De Roo, R.D., 2010. How does dew affect L-band backscatter? Analysis of pals data at the Iowa validation site and implications for SMAP. Int. Geosci. Remote Sens. Symp. 4835–4838 https://doi.org/10.1109/IGARSS.2010.5650792.

Hoskera, A.K., Nico, G., Ahmed, M.I., Whitbread, A., 2020. Accuracies of soil moisture estimations using a semi-empirical model over bare soil agricultural croplands from Sentinel-1 SAR data. Remote Sens. 12, 1–20. https://doi.org/10.3390/rs12101664.

Hosseini, M., McNairn, H., Merzouki, A., Pacheco, A., 2015. Estimation of Leaf Area Index (LAI) in corn and soybeans using multi-polarization C- and L-band radar data. Remote Sens. Environ. 170, 77–89. https://doi.org/10.1016/j.rse.2015.09.002.

Huang, S., Ding, J., Zou, J., Liu, B., Zhang, J., Chen, W., 2019. Soil moisture retrival based on sentinel-1 imagery under sparse vegetation coverage. Sensors (Switzerland) 19, 1–18. https://doi.org/10.3390/s19030589.

Ines, A.V.M., Das, N.N., Hansen, J.W., Njoku, E.G., 2013. Assimilation of remotely sensed soil moisture and vegetation with a crop simulation model for maize yield prediction. Remote Sens. Environ. 138, 149–164. https://doi.org/10.1016/j.rse.2013.07.018.

Jarlan, L., Mazzega, P., Mougin, E., 2002. Retrieval of land surface parameters in the Sahel from ERS wind scatterometer data: a "Brute force" method. IEEE Trans. Geosci. Remote Sens. 40 https://doi.org/10.1109/TGRS.2002.802500.

Jiang, L., Ma, E., Deng, X., 2014. Impacts of irrigation on the heat fluxes and near-surface temperature in an inland irrigation area of Northern China. Energies 7, 1300–1317. https://doi.org/10.3390/en7031300.

Jung, M., Reichstein, M., Schwalm, C.R., Huntingford, C., Sitch, S., Ahlström, A., Arneth, A., Camps-Valls, G., Ciais, P., Friedlingstein, P., Gans, F., Ichii, K., Jain, A.K., Kato, E., Papale, D., Poulter, B., Raduly, B., Rödenbeck, C., Tramontana, G., Viovy, N., Wang, Y.P., Weber, U., Zaehle, S., Zeng, N., 2017. Compensatory water effects link yearly global land CO 2 sink changes to temperature. Nature 541, 516–520. https://doi.org/10.1038/nature20780.

Karam, M.A., Fung, A.K., Lang, R.H., Chauhan, N.S., 1992. Microwave scattering model for layered vegetation. IEEE Trans. Geosci. Remote Sens. 30, 767–784. https://doi.org/10.1109/36.158872.

Karthikeyan, L., Pan, M., Wanders, N., Kumar, D.N., Wood, E.F., 2017. Four decades of microwave satellite soil moisture observations: part 1. A review of retrieval algorithms. Adv. Water Resour. 109, 106–120. https://doi.org/10.1016/j.advwatres.2017.09.006.

Kasischke, E.S., Bourgeau-chavez, L.L., Rober, A.R., Wyatt, K.H., Waddington, J.M., Turetsky, M.R., 2009. Remote sensing of environment effects of soil moisture and water depth on ERS SAR backscatter measurements from an Alaskan wetland complex. Remote Sens. Environ. 113, 1868–1873. https://doi.org/10.1016/j.rse.2009.04.006.

Kerr, Y.H., 2007. Soil moisture from space: where are we? Hydrogeol. J. 15, 117–120. https://doi.org/10.1007/s10040-006-0095-3.

Kerr, Y.H., Waldteufel, P., Wigneron, J.-P., Martinuzzi, J., Font, J., Berger, M., 2001. Soil moisture retrieval from space: the Soil Moisture and Ocean Salinity (SMOS) mission. IEEE Trans. Geosci. Remote Sens. 39, 1729–1735. https://doi.org/10.1109/36.942551.

Kerr, Y.H., Al-Yaari, A., Rodriguez-Fernandez, N., Parrens, M., Molero, B., Leroux, D., Bircher, S., Mahmoodi, A., Mialon, A., Richaume, P., Delwart, S., Al Bitar, A., Pellarin, T., Bindlish, R., Jackson, T.J., Rüdiger, C., Waldteufel, P., Mecklenburg, S., Wigneron, J.P., 2016. Overview of SMOS performance in terms of global soil moisture monitoring after six years in operation. Remote Sens. Environ. 180, 40–63. https://doi.org/10.1016/J.RSE.2016.02.042.

Khabbazan, S., Steele-Dunne, S.C., Vermunt, P., Judge, J., Vreugdenhil, M., Gao, G., 2022. The influence of surface canopy water on the relationship between L-band backscatter and biophysical variables in agricultural monitoring. Remote Sens. Environ. 268, 112789 https://doi.org/10.1016/j.rse.2021.112789.

Kim, D., Moon, H., Kim, H., Im, J., Choi, M., 2018. Intercomparison of downscaling techniques for satellite soil moisture products. Adv. Meteorol. 4832423. https://doi.org/10.1155/2018/4832423.

Koster, R.D., Dirmeyer, P.A., Guo, Z., Bonan, G., Chan, E., Cox, P., Gordon, C.T., Kanae, S., Kowalczyk, E., Lawrence, D., Liu, P., Lu, C.-H., Malyshev, S., McAvaney, B., Mitchell, K., Mocko, D., Oki, T., Oleson, K., Pitman, A., Sud, Y.C., Taylor, C.M., Verseghy, D., Vasic, R., Xue, Y., Yamada, T., 2004. Regions of strong coupling between soil moisture and precipitation. Science (80-.) 305, 1138–1141. https://doi.org/10.1126/science.1100217.

Koster, R.D., Guo, Z., Yang, R., Dirmeyer, P.A., Mitchell, K., Puma, M.J., 2009. On the nature of soil moisture in land surface models. J. Clim. 22, 4322–4335. https://doi.org/10.1175/2009JCLI2832.1.

Kustas, W.P., Zhan, X., Schmugge, T.J., 1998. Combining optical and microwave remote sensing for mapping energy fluxes in a semiarid watershed. Remote Sens. Environ. 64, 116–131. https://doi.org/10.1016/S0034-4257(97)00176-4.

Le Page, M., Toumi, J., Khabba, S., Hagolle, O., Tavernier, A., Hakim Kharrou, M., Er-Raki, S., Huc, M., Kasbani, M., El Moutamanni, A., Yousfi, M., Jarlan, L., 2014. A life-size and near real-time test of irrigation scheduling with a sentinel-2 like time series (SPOT4-Take5) in Morocco. Remote Sens. 6, 11182–11203. https://doi.org/10.3390/rs61111182.

Le Page, M., Jarlan, L., El Hajj, M.M., Zribi, M., Baghdadi, N., Boone, A., 2020. Potential for the detection of irrigation events on maize plots using Sentinel-1 soil moisture products. Remote Sens. 12, 1–22. https://doi.org/10.3390/rs12101621.

Le Page, M., Nguyen, T., Zribi, M., Boone, A., Dari, J., Modanesi, S., Zappa, L., Ouaadi, N., Jarlan, L., 2023. Irrigation timing retrieval at the plot scale using surface soil moisture derived from sentinel time series in Europe. Remote Sens. 15, 1449.

Lesiv, M., Laso Bayas, J.C., See, L., Duerauer, M., Dahlia, D., Durando, N., Hazarika, R., Kumar Sahariah, P., Vakolyuk, M., Blyshchyk, V., Bilous, A., Perez-Hoyos, A., Gengler, S., Prestele, R., Bilous, S., Akhtar, I.ul H., Singha, K., Choudhury, S.B., Chetri, T., Malek, Ž., Bungnamei, K., Saikia, A., Sahariah, D., Narzary, W., Danylo, O., Sturn, T., Karner, M., McCallum, I., Schepaschenko, D., Moltchanova, E., Fraisl, D., Moorthy, I., Fritz, S., 2019. Estimating the global distribution of field size using crowdsourcing. Glob. Chang. Biol. 25, 174–186. https://doi.org/10.1111/gcb.14492.

Li, F., Kustas, W.P., Anderson, M.C., Jackson, T.J., Bindlish, R., Prueger, J.H., 2006. Comparing the utility of microwave and thermal remote-sensing constraints in two-source energy balance modeling over an agricultural landscape. Remote Sens. Environ. 101, 315–328. https://doi.org/10.1016/j.rse.2006.01.001.

Li, Z., Liu, H., Zhao, W., Yang, Q., Yang, R., Liu, J., 2019. Estimation of evapotranspiration and other soil water budget components in an irrigated agricultural field of a desert oasis, using soil moisture measurements. Hydrol. Earth Syst. Sci. Discuss. 21, 4347–4361. https://doi.org/10.5194/hess-23-4685-2019.

Li, Z.L., Leng, P., Zhou, C., Chen, K.S., Zhou, F.C., Shang, G.F., 2021. Soil moisture retrieval from remote sensing measurements: current knowledge and directions for the future. Earth-Sci. Rev. 218, 103673 https://doi.org/10.1016/j.earscirev.2021.103673.

Long, D., Bai, L., Yan, L., Zhang, C., Yang, W., Lei, H., Quan, J., Meng, X., Shi, C., 2019. Generation of spatially complete and daily continuous surface soil moisture of high spatial resolution. Remote Sens. Environ. 233, 111364 https://doi.org/10.1016/j.rse.2019.111364.

Massari, C., Modanesi, S., Dari, J., Gruber, A.M., Lannoy, D., Girotto, M., Quintana-Seguí, P., Le Page, M., Jarlan, L., Zribi, M., Ouaadi, N., Vreugdenhil, M., Zappa, L., Dorigo, W., Wolfgang, W., Brombacher, J., Pelgrum, H., Jaquot, P., Freeman, V., Volden, E., Prieto, D.F., Tarpanelli, A., Barbetta, S., Brocca, L., 2021. A review of irrigation information retrievals from space and their utility for users. Remote Sens. 13 https://doi.org/10.3390/rs13204112.

Merlin, O., Rüdiger, C., Al Bitar, A., Richaume, P., Walker, J.P., Kerr, Y.H., 2012. Disaggregation of SMOS soil moisture in Southeastern Australia. IEEE Trans. Geosci. Remote Sens. 50, 1556–1571. https://doi.org/10.1109/TGRS.2011.2175000.

Merlin, O., Escorihuela, M.J., Mayoral, M.A., Hagolle, O., Al Bitar, A., Kerr, Y., 2013. Self-calibrated evaporation-based disaggregation of SMOS soil moisture: an evaluation study at 3 km and 100 m resolution in Catalunya, Spain. Remote Sens. Environ. 130, 25–38. https://doi.org/10.1016/J.RSE.2012.11.008.

Mishra, V., Cruise, J.F., Mecikalski, J.R., 2021. Assimilation of coupled microwave/thermal infrared soil moisture profiles into a crop model for robust maize yield estimates over Southeast United States. Eur. J. Agron. 123, 126208 https://doi.org/10.1016/j.eja.2020.126208.

Mladenova, I., Lakshmi, V., Jackson, T.J., Walker, J.P., Merlin, O., de Jeu, R.A.M., 2011. Validation of AMSR-E soil moisture using L-band airborne radiometer data from National Airborne Field Experiment 2006. Remote Sens. Environ. 115, 2096–2103. https://doi.org/10.1016/j.rse.2011.04.011.

Moran, M.S., Peters-Lidard, C.D., Watts, J.M., Mc Elroy, S., 2004. Estimating soil moisture at the watershed scale with satellite-based radar and land surface models. Can. J. Remote. Sens. 30, 805–826. https://doi.org/10.5589/m04-043.

Morrison, K., Wagner, W., 2020. Explaining anomalies in SAR and scatterometer soil moisture retrievals from dry soils with subsurface scattering. IEEE Trans. Geosci. Remote Sens. 58, 2190–2197. https://doi.org/10.1109/TGRS.2019.2954771.

Motte, E., Zribi, M., Fanise, P., Egido, A., Darrozes, J., Al-Yaari, A., Baghdadi, N., Baup, F., Dayau, S., Fieuzal, R., Frison, P.L., Guyon, D., Wigneron, J.P., 2016. GLORI: a GNSS-R dual polarization airborne instrument for land surface monitoring. Sensors (Switzerland) 16, 1–21. https://doi.org/10.3390/s16050732.

Nijssen, B., Schnur, R., Lettenmaier, D.P., 2001. Global retrospective estimation of soil moisture using the variable infiltration capacity land surface modl, 1980-93. J. Clim. 14, 1790–1808. https://doi.org/10.1175/1520-0442(2001)014<1790:GREOSM>2.0.CO;2.

NISAR, 2019. NISAR: The NASA-ISRO SAR Mission. Pasadena, California.

Njoku, E.G., 2004. AMSR-E/Aqua Daily L3 Surface Soil Moisture, Interpretive Parameters, & QC EASE-Grids, Version 2. Boulder, Colorado, USA. https://doi.org/10.5067/AMSR-E/AE_LAND3.002.

Njoku, E.G., Jackson, T.J., Lakshmi, V., Chan, T.K., Nghiem, S.V., 2003. Soil moisture retrieval from AMSR-E. IEEE Trans. Geosci. Remote Sens. 41, 215–228. https://doi.org/10.1109/TGRS.2002.808243.

Nolin, M., Quenum, M., Cambouris, A., Martin, A., Cluis, D., 2005. Rugosité de la surface du sol – description et interprétation. Agrosol 16, 5–21.

Oh, Y., Sarabandi, K., Ulaby, F.T., 1992. An empirical model and an inversion technique for radar scattering from bare soil surfaces. IEEE Trans. Geosci. Remote Sens. 30, 370–381. https://doi.org/10.1109/36.134086.

Ojha, N., Merlin, O., Molero, B., Suere, C., Olivera-guerra, L., Hssaine, B.A., Amazirh, A., Al Bitar, A., Escorihuela, M.J., Er-raki, S., 2019. Stepwise disaggregation of SMAP soil moisture at 100 m resolution using Landsat-7 / 8 data and a varying intermediate resolution. Remote Sens. 11, 1863. https://doi.org/10.3390/rs11161863.

Ojha, N., Merlin, O., Amazirh, A., Ouaadi, N., Rivalland, V., Jarlan, L., Er-raki, S., Escorihuela, M.J., 2021. A calibration / disaggregation coupling scheme for retrieving soil moisture at high Spatio-temporal resolution: synergy optical / thermal and Sentinel-1 radar data. Sensors 21, 7406. https://doi.org/10.3390/s21217406.

Ouaadi, N., Jarlan, L., Ezzahar, J., Zribi, M., Khabba, S., Bouras, E., Bousbih, S., Frison, P., 2020. Monitoring of wheat crops using the backscattering coe ffi cient and the interferometric coherence derived from Sentinel-1 in semi-arid areas. Remote Sens. Environ. 251, 112050 https://doi.org/10.1016/j.rse.2020.112050.

Ouaadi, N., Jarlan, L., Khabba, S., Ezzahar, J., Le Page, M., Merlin, O., 2021. Irrigation amounts and timing retrieval through data assimilation of surface soil moisture into the FAO-56 approach in the South Mediterranean region. Remote Sens. 13, 2667.

Ouaadi, N., Ezzahar, J., Khabba, S., Er-Raki, S., Chakir, A., Ait Hssaine, B., Le Dantec, V., Rafi, Z., Beaumont, A., Kasbani, M., Jarlan, L., 2021a. C-band radar data and in situ measurements for the monitoring of wheat crops in a semi-arid area (center of Morocco). Earth Syst. Sci. Data 13, 3707–3731. https://doi.org/10.5194/essd-13-3707-2021.

Paolini, G., Escorihuela, M.J., Bellvert, J., Merlin, O., 2022a. Disaggregation of SMAP soil moisture at 20 m resolution: validation and sub-field scale analysis. Remote Sens. 14, 1–16. https://doi.org/10.3390/rs14010167.

Paolini, G., Escorihuela, M.J., Merlin, O., Sans, M.P., Bellvert, J., 2022b. Classification of different irrigation Systems at Field Scale Using Time-Series of remote sensing data. IEEE J. Sel. Top. Appl. Earth Obs. Remote Sens. 15, 10055–10072. https://doi.org/10.1109/JSTARS.2022.3222884.

Peng, J., Loew, A., Merlin, O., Verhoest, N.E.C., 2017. A review of spatial downscaling of satellite remotely sensed soil moisture. Rev. Geophys. 55, 341–366. https://doi.org/10.1002/2016RG000543.

Peng, J., Albergel, C., Balenzano, A., Brocca, L., Cartus, O., Cosh, M.H., Crow, W.T., Dabrowska-Zielinska, K., Dadson, S., Davidson, M.W.J., de Rosnay, P., Dorigo, W., Gruber, A., Hagemann, S., Hirschi, M., Kerr, Y.H., Lovergine, F., Mahecha, M.D., Marzahn, P., Mattia, F., Musial, J.P., Preuschmann, S., Reichle, R.H., Satalino, G.,

Silgram, M., van Bodegom, P.M., Verhoest, N.E.C., Wagner, W., Walker, J.P., Wegmüller, U., Loew, A., 2021. A Roadmap for High-Resolution Satellite Soil Moisture Applications – Confronting Product Characteristics With.

Picard, G., Toan, T.L., 2002. A multiple scattering model for c-band backscatter of wheat canopies. J. Electromagn. Waves Appl. 16, 1447–1466. https://doi.org/10.1163/156939302X00093.

Qu, Y., Zhu, Z., Montzka, C., Chai, L., Liu, S., Ge, Y., Liu, J., Lu, Z., He, X., Zheng, J., Han, T., 2021. Inter-comparison of several soil moisture downscaling methods over the Qinghai-Tibet Plateau, China. J. Hydrol. 592, 125616 https://doi.org/10.1016/j.jhydrol.2020.125616.

Riedel, T., Pathe, C., Thiel, C., Herold, M., Schmullius, C., 2002. Systematic investigation on the effect of dew and interception on multifrequency and multipolarimetric radar backscatter signals. In: 3rd International Symposium, 'Retrieval of Bio- and Geo-Physical Parameters from SAR Data for Land Applications', pp. 99–104.

Ritzema, H.P., Satyanarayana, T.V., Raman, S., Boonstra, J., 2008. Subsurface drainage to combat waterlogging and salinity in irrigated lands in India: lessons learned in farmers' fields. Agric. Water Manag. 95, 179–189. https://doi.org/10.1016/j.agwat.2007.09.012.

Rojas-Briales, E., 2000. Socio-economics of nature protection policies in the perspective of the implementation of Natura 2000 network: the Spanish case. Forestry 73, 199–207. https://doi.org/10.1093/forestry/73.2.199.

Rüdiger, C., Calvet, J.C., Gruhier, C., Holmes, T.R.H., de Jeu, R.A.M., Wagner, W., 2009. An intercomparison of ERS-Scat and AMSR-E soil moisture observations with model simulations over France. J. Hydrometeorol. 10, 431–447. https://doi.org/10.1175/2008JHM997.1.

Sabaghy, S., Walker, J.P., Renzullo, L.J., Akbar, R., Chan, S., Chaubell, J., Das, N., Dunbar, R.S., Entekhabi, D., Gevaert, A., Jackson, T.J., Loew, A., Merlin, O., Moghaddam, M., Peng, Jian, Peng, Jinzheng, Piepmeier, J., Rüdiger, C., Stefan, V., Wu, X., Ye, N., Yueh, S., 2020. Comprehensive analysis of alternative downscaled soil moisture products. Remote Sens. Environ. 239, 111586 https://doi.org/10.1016/j.rse.2019.111586.

Schmugge, T., 1978. Remote sensing of surface soil moisture. J. Appl. Meteorol. https://doi.org/10.1175/1520-0450(1978)017<1549:RSOSSM>2.0.CO;2.

Schmugge, T.J., 1983. Remote sensing of soil moisture: recent advances. IEEE Trans. Geosci. Remote Sens. GE-21, 336–344. https://doi.org/10.1109/TGRS.1983.350563.

Subhani, A., Tariq, M., Jafar, M.S., Latif, R., Khan, M., Iqbal, Muhammad Sajid, Iqbal, Muhammad Shahid, 2012. Role of soil moisture in fertilizer use efficiency for Rainfed areas-a review. J. Biol. Agric. Healthc. 2, 1–9.

Ulaby, F.T., Long, D.G., 2014. Microwave Radar and Radiometric Remote Sensing. The University of Michigan Press.

Ulaby, F.T., Abdelrazik, M., Stiles, W.H., 1984. Snowcover influence on backscattering from terrain. IEEE Trans. Geosci. Remote Sens. GE-22, 126–133. https://doi.org/10.1109/TGRS.1984.350604.

Ulaby, F.T., Moore, R.K., Fung, A.K., 1986. Microwave Remote Sensing: Active and Passive, Volume III-from Theory to Applications.

Ulaby, F.T., Sarabandi, K., McDonald, K., Whitt, M., Craig Dobson, M., 1990. Michigan microwave canopy scattering model. Int. J. Remote Sens. 11, 1223–1253. https://doi.org/10.1080/01431169008955090.

Ulaby, F.T., Dubois, P.C., Jakob, V.Z., 1996. Radar mapping of surface soil moisture. J. Hydrol. 184, 57–84.

Van Den Hurk, B., 2001. Energy balance based surface flux estimation from satellite data, and its application for surface moisture assimilation. Meteorog. Atmos. Phys. 76, 43–52. https://doi.org/10.1007/s007030170038.

Vereecken, H., Huisman, J.A., Pachepsky, Y., Montzka, C., van der Kruk, J., Bogena, H., Weihermüller, L., Herbst, M., Martinez, G., Vanderborght, J., 2014. On the spatio-temporal dynamics of soil moisture at the field scale. J. Hydrol. 516, 76–96. https://doi.org/10.1016/J.JHYDROL.2013.11.061.

Verhoef, A., 2004. Remote estimation of thermal inertia and soil heat flux for bare soil. Agric. For. Meteorol. 123, 221–236. https://doi.org/10.1016/j.agrformet.2003.11.005.

Wagner, W., Noll, J., Borgeaud, M., Rott, H., 1999. Monitoring soil moisture over the Canadian prairies with the ERS scatterometer. IEEE Trans. Geosci. Remote Sens. 37, 206–216. https://doi.org/10.1109/36.739155.

Wagner, W., Scipal, Klaus, Pathe, Carsten, Gerten, Dieter, Lucht, Wolfgang, Rudolf, Bruno, Wagner, C., Scipal, K., Pathe, C., Gerten, D., Lucht, W., Rudolf, B., 2003. Evaluation of the agreement between the first global remotely sensed soil moisture data with model and precipitation data. J. Geophys. ResRes 108, 4611. https://doi.org/10.1029/2003JD003663.

Wagner, W., Hahn, S., Kidd, R., Melzer, T., Bartalis, Z., Hasenauer, S., Figa-Saldaña, J., De Rosnay, P., Jann, A., Schneider, S., Komma, J., Kubu, G., Brugger, K., Aubrecht, C., Züger, J., Gangkofner, U., Kienberger, S., Brocca, L., Wang, Y., Blöschl, G., Eitzinger, J., Steinnocher, K., Zeil, P., Rubel, F., 2013. The ASCAT soil moisture product: a review of its specifications, validation results, and emerging applications. Meteorol. Z. 22, 5–33. https://doi.org/10.1127/0941-2948/2013/0399.

Wagner, W., Lindorfer, R., Melzer, T., Hahn, S., Bauer-Marschallinger, B., Morrison, K., Calvet, J.C., Hobbs, S., Quast, R., Greimeister-Pfeil, I., Vreugdenhil, M., 2022. Widespread occurrence of anomalous C-band backscatter signals in arid environments caused by subsurface scattering. Remote Sens. Environ. 276, 113025 https://doi.org/10.1016/j.rse.2022.113025.

Walker, J.P., Houser, P.R., Willgoose, G.R., 2004a. Active microwave remote sensing for soil moisture measurement: a field evaluation using ERS-2. Hydrol. Process. https://doi.org/10.1002/hyp.1343.

Walker, J.P., Willgoose, G.R., Kalma, J.D., 2004b. In situ measurement of soil moisture: a comparison of techniques. J. Hydrol. 293, 85–99. https://doi.org/10.1016/j.jhydrol.2004.01.008.

Wang, K., Dickinson, R.E., 2012. A review of global terrestrial evapotranspiration: observation, modeling, climatology, and climatic variability. Rev. Geophys. 50 https://doi.org/10.1029/2011RG000373.

Wang, Y., Kasischke, E.S., Bourgeau-Chavez, L.L., O'neill, K.P., French, N.H.F., 2000. Assessing the influence of vegetation cover on soil-moisture signatures in fire-disturbed boreal forests in interior Alaska: modelled results. Int. J. Remote Sens. 21, 689–708. https://doi.org/10.1080/014311600210515.

Wang, X., Piao, S., Ciais, P., Friedlingstein, P., Myneni, R.B., Cox, P., Heimann, M., Miller, J., Peng, S., Wang, T., Yang, H., Chen, A., 2014. A two-fold increase of carbon cycle sensitivity to tropical temperature variations. Nature 506, 212–215. https://doi.org/10.1038/nature12915.

Wang, C., Zhang, Z., Paloscia, S., Zhang, H., Wu, F., Wu, Q., 2018. Permafrost soil moisture monitoring using multi-temporal TerraSAR-X data in Beiluhe of northern Tibet, China. Remote Sens. 10, 1577. https://doi.org/10.3390/RS10101577.

Weiss, M., Jacob, F., Duveiller, G., 2020. Remote sensing for agricultural applications : a meta-review. Remote Sens. Environ. 236, 111402 https://doi.org/10.1016/j.rse.2019.111402.

Yin, J., Zhan, X., Liu, J., Schull, M., 2019. An Intercomparison of Noah model skills with bene fi ts of assimilating SMOPS blended and individual soil moisture retrievals. Water Resour. Res. 55, 2572–2592. https://doi.org/10.1029/2018WR024326.

Zhang, D., Zhou, G., 2016. Estimation of soil moisture from optical and thermal remote sensing: a review. Sensors (Switzerland) 16. https://doi.org/10.3390/s16081308.

Zheng, X., Feng, Z., Li, L., Li, B., Jiang, T., Li, Xiaojie, Li, Xiaofeng, Chen, S., 2021. Simultaneously estimating surface soil moisture and roughness of bare soils by combining optical and radar data. Int. J. Appl. Earth Obs. Geoinf. 100, 102345 https://doi.org/10.1016/j.jag.2021.102345.

Zonno, Mariantonietta, Matar, Jalal, de Almeida, Felipe Queiroz, Younis, Marwan, Reimann, Jens, Rodriguez-Cassola, Marc, Krieger, Gerhard, Perrera, Andrea, Tossaint, Michel, 2021. Sentinel-1 Next Generation: main mission and instrument performance of the Phase 0. In: 13th European Conference on Synthetic Aperture Radar (EUSAR2021).

Zribi, M., Dehaye, V., Dassas, K., Fanise, P., Le Page, M., Laluet, P., Boone, A., 2022. Airborne GNSS-R polarimetric multiincidence data analysis for surface soil moisture estimation over an agricultural site. IEEE J. Sel. Top. Appl. Earth Obs. Remote Sens. 15, 8432–8441. https://doi.org/10.1109/JSTARS.2022.3208838.